SiGe/Si Heterojunction Internal Photoemission Separate Absorption and Multiplication Avalanche Middle Wavelength Infrared Photodiode

by

Yuan Zhang

A thesis
presented to the University of Waterloo
in fulfilment of the
thesis requirement for the degree of
Master of Applied Science
in
Electrical and Computer Engineering

Waterloo, Ontario, Canada, 2014

I hereby declare that I am the sole author of this thesis. This is a true copy of the thesis, including any required final revisions, as accepted by my examiners. I understand that my thesis may be made electronically available to the public.

Acknowledgments

I would like to thank my supervisor, Prof. A.Sazonov for guiding me throughout my term as a graduate student

I am thankful to all my present and past group members for helping me at various stages.

I want to thank to my mother (ShuZhi Ji) and father (WenTong Zhang) who always trusted in me and supported me in all my decisions.

I want to thank Juan Ding for her love and support, without her it would not have been easy to finish my thesis. Finally, love to my son Micheal Zhang who always fills me with enthusiasm and delight.

Abstract

Separate-absorption-and-multiplication (SAM) Avalanche PhotoDiode (APD) is widely accepted in optical communication systems due to the presence of large photocurrent gain. In this thesis, a designed SAM middle wavelength infrared avalanche photo detector operating at room temperature is presented. The designed photo detector is based on SiGe/Si heterojunction internal photoemission (HIP) and it is compatible with CMOS technology. The detection mechanism of the SiGe/Si HIP detector is infrared absorption in the degenerately doped p+-SiGe layer followed by internal photoemission of photoexcited holes over the heterojunction barrier. Silvaco TCAD tool is utilized to implement the simulation of this designed SiGe/Si HIP SAM APD. The structure of the designed APD is evaluated by simulation tools, the simulation results of the dark current, the current under illumination, photo-generation rate, recombination rate, and electrical field are shown in this thesis. The relation between dark current and generation-recombination is discussed at the end of this thesis.

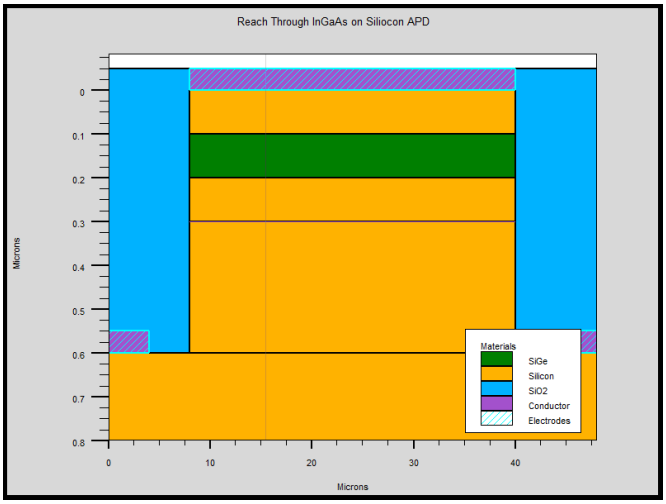

Key word: *SAM APD, Infrared, Room Temperature, SiGe/Si HIP, Silvaco TCAD, photo-generation rate, recombination rate, and dark current, etc.*

Contents

Definitions:

HIP: Heterojunction Internal Photoemission

APD: Avalanche Photodiode

TCAD: Technology Computer Aided Design

FPA: Focal Plane Array

CCD: Charged Couple Device

MIS: Metal-Insulator-Semiconductor

List of figures

Chapter 1 Introduction of Infrared and Photodiode

1.1 An Introduction to Infrared Photodetectors

Infrared detector systems are used to monitor environmental factors and the weather, make astronomical observations, and perform medical diagnostics. These systems are frequently built as focal plane arrays, which consist of as many as millions of individual photodetectors [1, 2].

Future infrared photodetector systems must possess reduced cooling requirements, consume less power, exhibit longer lifetimes, and have improved manufacturing ability. The best performing infrared photodetectors are currently cooled to cryogenic temperatures, which enables optimal operation by decreasing internal detector noise [3]. Infrared photodetector operating in higher temperature will enable the use of lower cost coolers with decreased power requirements. This is anticipated to permit more extensive field use and result in a decrease of the critical wait timing between powering on the imaging system and being able to detect the image. Increasing the yields and simplifying the fabrication requirements of the detector arrays will result in substantial cost savings [2, 4, and 5].

1.2 Emission and Atmospheric Transmission of Infrared Radiation

Infrared detectors monitor thermal radiators, and these may be approximated as blackbody sources. The greater the thermal energy of the object, the higher the energies of the emitted photons. The spectral radiant existence of a blackbody source, Meλ(λ,T) is obtained from the Planck radiation law, and may be expressed as:

$$M_{e,\lambda}(\lambda, T) = \frac{2\pi hc^2}{\lambda^5}\left[\exp\left(\frac{hc}{\lambda kT}\right) - 1\right]^{-1}$$

where λ is the wavelength, h is Planck's constant, c is the velocity of light, and k is Boltzmann's constant. As plotted in Figure 1.1, the peak power emitted by hotter objects occurs at lower wavelengths, while the power emitted at all wavelengths increases. The spectral window spanning 2 to 12 microns coincides with a majority of the radiation emitted by objects near room temperature.

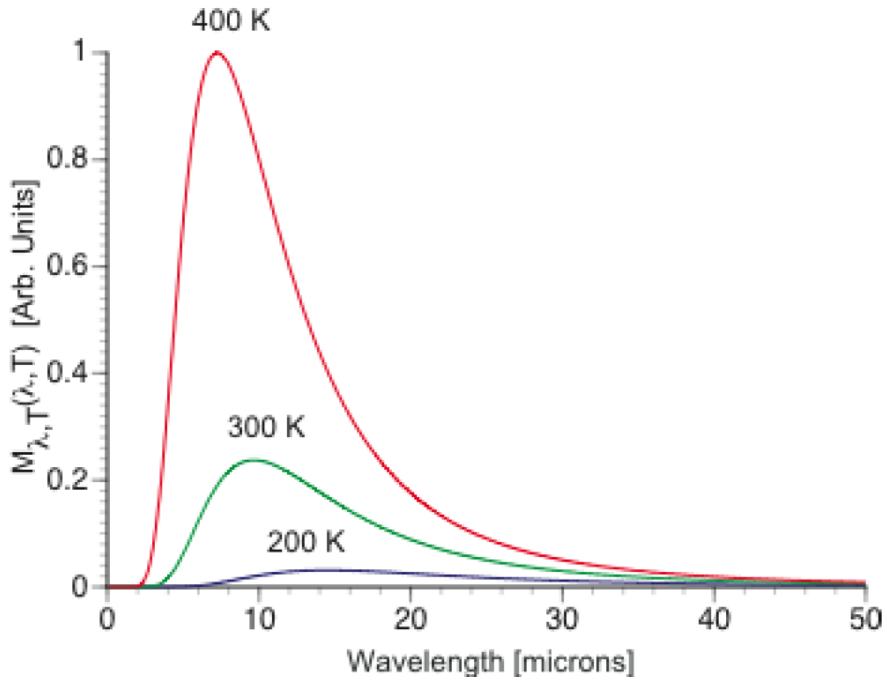

Figure 1.1 Emissions and Atmospheric Transmission of Infrared Radiation[6]

Infrared photodetection systems are often used as remote sensors, which has led to infrared detectors commonly being designed to operate in one of two atmospheric transmission windows as shown in Figure 1.2: the 3-5 micron medium wavelength infrared (MWIR) window or the 8-14 micron long wavelength infrared (LWIR) window. Operation in the MWIR atmospheric window is typical when the application relies on contrast resolution more than detector sensitivity, comparatively hot objects are monitored, and operation occurs during clear weather. High humidity conditions do not affect the atmospheric transmission of radiation in this window; however the LWIR range is better suited for foggy, hazy, dusty, or misty conditions [1].

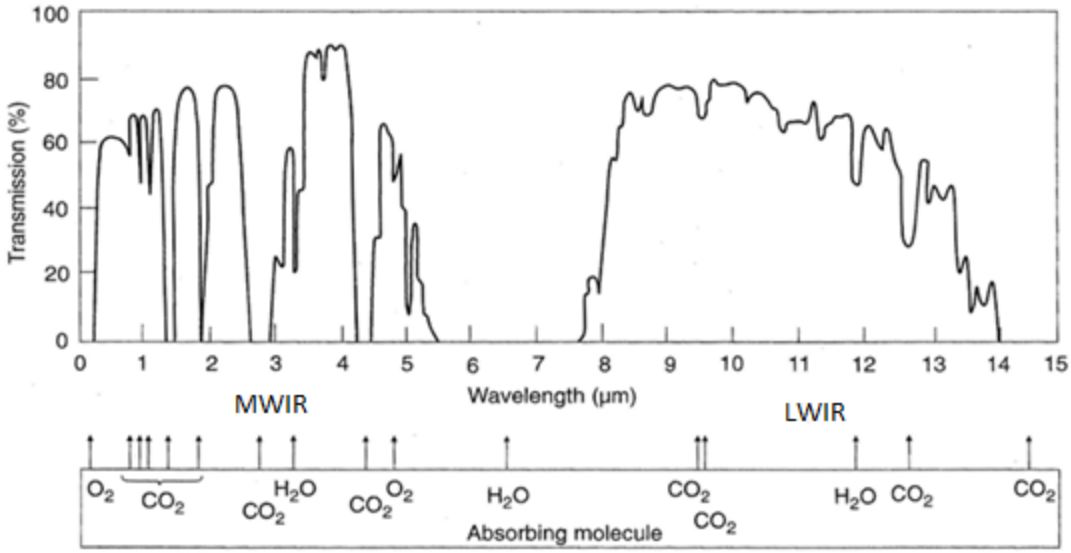

Figure 1.2 IR Detector two operating windows [6]

1.3 Noise in Semiconductor-Based MWIR Photodetectors

Noise in infrared detection systems is attributable to statistical fluctuations in the detected signal as well as fluctuations in the flow of spurious charge carriers created through means other than by the absorption of a signal photon, such as through thermal processes. Thermal processes are particularly important for narrow bandgap semiconductor based photodetectors operating near room temperature, as the energy of the charge carriers, kT, is comparable to the transition energy [3]. Some common types of internal noise in infrared detectors are Johnson-Nyquist, 1/f, generation-recombination, diffusion, tunneling, and surface leakage [19,23]. Noise may also arise through external sources such as background radiation, cooling irregularities, mechanical issues, and incident optical sources [23,25].

Random motion of carriers in a semiconductor results in fluctuations of the open circuit voltage, V_j, called thermal or Johnson-Nyquist noise [24],

$$V_j = \sqrt{4kTR\Delta f}$$

with Δf representing the electrical bandwidth, and R the real part of the impedance.

More precisely written 1/fα, with α having a value of approximately unity, 1/f noise is sometimes correlated with surface effects and is important at lower frequencies. It has not been modeled precisely [24,25].

Shot noise has a white spectrum at low frequencies and arises as a consequence of the quantum fluctuations of the optical field, as well as statistical variations in the emission, recombination, and flow of charge carriers. The mean square shot noise current, I_n, is modeled as [24]

$$I_n = \sqrt{2q\bar{I}\Delta f}$$

with I the current, and q the electronic charge.

The components of dark current important to this work are due to surface leakage, generation processes, and those produced by the detection of background radiation. These may be modeled as shot noise [19].

Recombination processes are not significant for photodiodes and Barrier photodetectors. Recombination processes become important in the presence of excess carriers, as in the case of photoconductors and when carriers are injected into a device. Generation processes, and not recombination processes, are considered in devices without excess carriers, which is the case for devices that extract carriers, such as photodiodes [19,26]. The characteristics of generation noise depend on the constituent detector material, device structure, and device temperature [27]. The three most important types of generation mechanisms in narrow-bandgap semiconductors are: Shockley-Read-Hall, Auger, and radiative. Equation below is a general formalism applicable to variety of semiconductor generation processes. The generation rate, G_k, of a particular mechanism, k, is related to the square of the intrinsic carrier

concentration, n_i, through a proportionality term, g_k.

$$G_k = g_k\left(n_i^2\right).$$

The net generation rate, G, is the sum of all G_k. The square of the intrinsic carrier concentration is the product of the electron, n_o, and hole, p_o, concentrations under conditions of thermal equilibrium: $n_i^2 = n_o\, p_o$. Non-equilibrium carrier densities are $n = n_i + \delta n$, and $p = p_i + \delta p$. The general expressions for the electron, n, and hole, p, concentrations are:

$$n = N_c F_{1/2}\left[-\frac{\left(E_c - E_f\right)}{kT}\right]$$

$$p = N_v F_{1/2}\left[-\frac{\left(E_f - E_v\right)}{kT}\right]$$

with the Fermi-Dirac integral, F1/2[η], defined using

$$F_j(\eta) = \frac{1}{\Gamma(j+1)}\int_0^\infty \frac{x^j\, dx}{1+\exp(x-\eta)},$$

where Γ represents the gamma function, and the effective densities of states in the conduction and valence bands, N_c and N_v respectively, are

$$N_c = 2\left(\frac{m_e^* kT}{2\pi\hbar^2}\right)^{3/2}$$

$$N_v = 2\left(\frac{m_h^* kT}{2\pi\hbar^2}\right)^{3/2}$$

with electron and hole effective masses, m_e^* and m_h^*. In this work, when treating the case of degenerate semiconductors, the Fermi-Dirac integral is approximated as [29]

$$F_{1/2}(\eta) \approx \left[\exp(-\eta) + \frac{3\pi^{1/2}/4}{\left(\eta^4 + 33.6\eta\left\{1 - 0.68\exp\left[-0.17(\eta+1)^2\right]\right\} + 50\right)^{3/8}} \right]^{-1}$$

which valid over ??<η<?. In the case of non-degenerate semiconductors the form

$$F_{1/2}(\eta) \approx \exp(\eta)$$

is used.

The net generation rate of the process k, becomes, under small-signal conditions and expressed in terms of the lifetime of the process, τ_k,

$$G_k = \frac{\delta n}{\tau_k}$$

with the overall recombination lifetime the parallel sum

$$\frac{1}{\tau} = \sum_k \frac{1}{\tau_k}.$$

1.4 Noise in MWIR Photodetectors

The main noise sources in the MWIR Photodetectors are Shockley-Read-Hall Noise, Auger Noise and Radiative Recombination.

1.4.1 Shockley-Read-Hall Noise

Shockley-Read-Hall generation-recombination processes are extrinsic, as they utilize energy levels within the bandgap resulting from impurities and material defects. Electrons and holes may be both captured by and emitted from these trap states, which impacts excess carrier lifetimes. Semiconductor material with better crystalline quality exhibits less SRH generation current. The net generation rate, which takes into account all four processes, is [7],

$$G_{SRH} = \frac{\sigma_n \sigma_p v_{th} n_i^2 N_{DL}}{\sigma_n (n + n_1) + \sigma_p (p + p_1)} \quad (1.3.1)$$

with σ_n and σ_p the electron and hole capture cross sections, v_{th} the carrier thermal velocity, N_{DL} the density of the traps, and the nondegenerate electron, n_l, and hole, p_l, concentrations corresponding to a Fermi energy level coincident with the energy of the traps, E_T, are

$$n_1 = N_c \exp\left[-\frac{(E_c - E_T)}{kT}\right]$$

$$p_1 = N_v \exp\left[-\frac{(E_T - E_v)}{kT}\right]$$

The most efficient generation of SRH current occurs when the energies of the trap states and the Fermi level coincide near the middle of the bandgap. It is of particular interest to note the Fermi energy lies in the middle of the bandgap in the depletion region of p-n junction photodetectors, and SRH generation current is a primary noise source for cooled photodiodes.

It is useful to simplify above Equation by approximating terms n, p, n_l, and p_l for cases in which the Fermi level is located at mid-gap in the depletion region of a semiconductor device. The approximation substitutes $E_g/2kT$ for the arguments in the exponentials of each of these four terms. Doing so allows n, p, n_l, and p_l to be easily summed and G_{SRH} to be expressed, as G_{SRH}^{DPEL}, in terms of the intrinsic carrier concentration and a lifetime, τ_o:

$$G_{SRH}^{depl} \approx \frac{n_i^2}{\tau_o \sqrt{N_c N_v} \exp\left(-\frac{E_g/2}{kT}\right)} = \frac{n_i}{\tau_o}$$

Where

$$\tau_o = \left(\frac{\sigma_n \sigma_p v_{th} N_{DL} \sqrt{N_c N_v}}{2\sigma_n N_c + 2\sigma_p N_v} \right)^{-1}$$

The relation between the bandgap energy, temperature, and G_{SRH}^{DPEL} is:

$$G_{SRH}^{depl} \propto T^{1/2} n_i \propto T^2 \exp\left(-\frac{E_g}{2kT} \right)$$

which takes into account the $T^{1/2}$ temperature dependence of the thermal velocity [24] in the lifetime term.

1.4.2 Auger Noise

Multiple types of band-to-band Auger processes are possible in semiconductor materials [33]. Auger Noise involves two transitions: one between the conduction and heavy-hole bands, and the other between two energy states in the conduction band.

1.4.3 Radiative Recombination noise

Radiative recombination occurs when a photon is emitted upon the recombination of an electron and a hole. In direct bandgap semiconductor-based light emitting diodes, the intrinsic radiative recombination process occurring across the bandgap is important. Radiative recombination is not considered a limiting factor in practical photodetectors. Most photons arising through radiative decay are reabsorbed, which lengthens the measured radiative lifetime. An expression for the radiative lifetime, τ_R, is [7]

$$\tau_R = \frac{n_i^2}{G_R (n_o + p_o)}$$

Auger and radiative recombination are intrinsic processes for which universal curves

of the associated lifetimes, such as those shown in Figure 1.3, may be generated. Universal curves may not be produced for the lifetimes of SRH processes, as these depend on the density of traps.

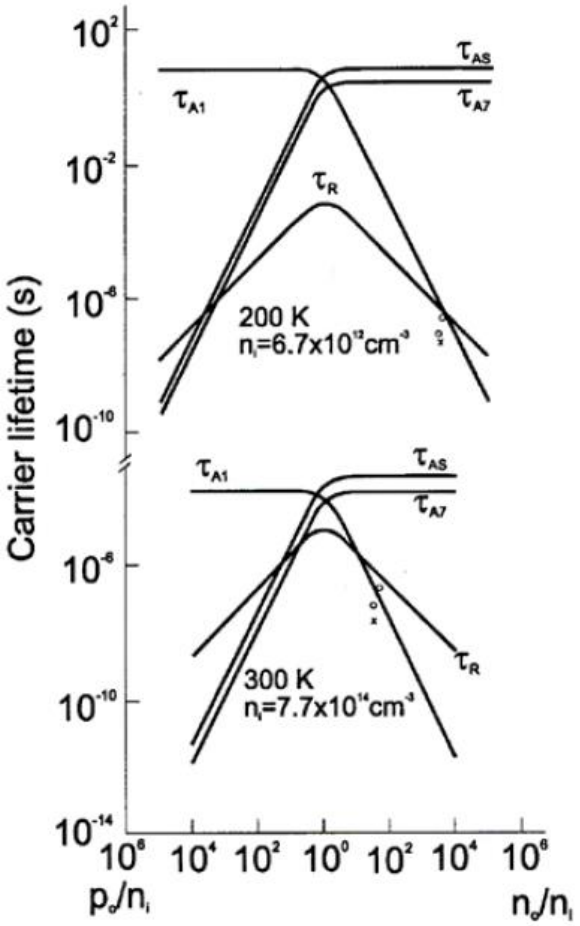

Figure 1.3 Carrier lifetime of Auger and radiative processes in InAs [6]

1.5 Figures of Merit

Figures of merit quantify the performance of an infrared detection system; they contrast the numbers of carriers created by incident signal photons with the numbers generated from noise processes. The most useful figures of merit allow comparison of infrared detection systems with different architectures, constituent material systems, and manufacturers. While some figures of merit are broadly applicable, none is universally appropriate. In some cases, experimental conditions influence the reported

numerical values [2].

Most of the figures of merit applied to infrared detection systems use the signal to noise ratio, SNR, as a basis, and are therefore related to one another. One expression of SNR,2

$$SNR = \frac{I_s}{I_n}$$

is the ratio of the signal current, Is, and the noise current, In the responsivity, R_i, is the frequency dependent ratio of the output photocurrent, I_s, to the incident optical power, [24,26]

$$R_i = \frac{I_s}{P_{opt}} = \frac{\eta q}{h\nu} = \eta \frac{q\lambda}{hc}$$

in which ν is the frequency of light, and the quantum efficiency, η, is defined as the number of electron-hole pairs generated for each incident photon. The value of the quantum efficiency strongly depends on the absorption coefficient of the material, α(λ) [24]. Responsivity is a more attractive metric when the ratio is linear, but it is not as useful as some other figures of merit as it contains no information about the minimum strength a signal must have to be detectable [37].

1.6 Classes of Infrared Photodetectors

Infrared detectors are classified as either photon or thermal detectors. Thermal detectors experience changes in electrical properties when the temperature of the constituent material changes after absorbing infrared radiation; In photon-based detectors, incident photons interact directly with electrons. This results in a modification of the electronic distribution in the material and the alteration of an electronic property [1, 41].

Microbolometers, which are members of the thermal class of detectors, and p-n junction photodiodes, which are photon-based detectors, are currently the most widely used Infrared Photodetectors.

1.6.1 Thermal Detectors

The three types of thermal detectors are bolometers, pyroelectric detectors, and sensors based on the thermoelectric effect such as thermocouples. Electrical resistance changes with temperature in bolometers, differences in the spontaneous electrical polarization are monitored in pyroelectric detectors, and variable voltage generation is the basis of thermocouples. These, like all thermal detectors, return a signal based on the radiant power incident on the detector and are largely insensitive to the spectral content of the radiation. The majority of thermal detectors are not cooled, which makes them inexpensive, easy to use, and favored for use in space-based and field operations. (Thermal photodetectors based on superconductors, which are cooled to tens of kelvin, are a significant exception.) Benefits associated with uncooled operation are offset by slow response times, which is a consequence of the necessary wait while the material heats and cools, and their sensitivities well below those of photon-based detectors [2,19]

Micromachined bolometers, termed microbolometers, have been fabricated and fashioned into uncooled FPAs with monolithic and hybrid readout circuits [2, 5]. Infrared detector systems based on microbolometer FPAs are becoming increasingly important for LWIR detection for applications such as surveillance, night vision, and thermal sights. Microbolometer arrays with 640 x 480 elements and pixels with 17 micron side lengths are commercially available [42].

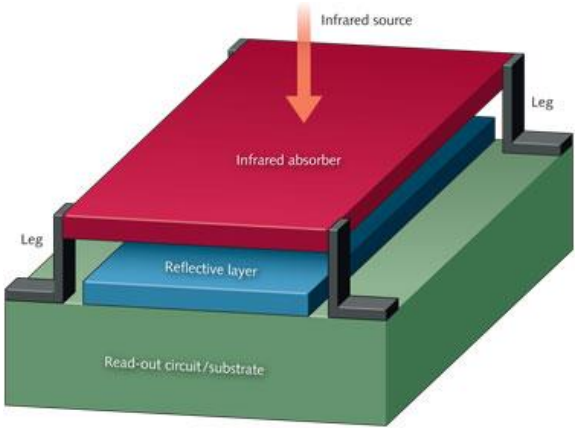

Figure 1.4 Microbolometer [65]

1.6.2 Photon Detectors

The class of photon-based detectors includes semiconductor-based infrared detectors. Carriers generated in photoconductive detectors alter the conductivity of the material, while electron-hole pairs created in photovoltaic detectors result in a photocurrent or a voltage difference detectable across two electrodes. Energy states residing in the bandgap of the host semiconductor may be created by doping a semiconductor with impurity atoms. The extrinsic absorption of a photon involves exciting a carrier from such a state into an energy band of the semiconductor, and these transitions are used in some photoconductive detectors. Internal photoemission, which referrs to the photon-induced ejection of an electron, is the basis of Schottky barrier detector operation. Quantized energy levels may be created with a quantum well structure, and transitons involving these levels have been used in photoconductive and photovoltaic detectors [7, 43].

Unlike the majority of thermal detectors, photon-based detectors exhibit pronounced wavelength dependence. For photon-based detectors there exists an abrupt long wavelength cutoff and a typically more gradual drop off in responsivity for shorter wavelengths [7, 24]. Detection occurs when the photons composing the incident

radiation possess enough energy to transition carriers into different energy states. In the case of intrinsic photoconductive and photovoltaic detectors, carriers are excited across the bandgap of the semiconductor. The long wavelength cutoff,

$$\lambda_c = \frac{hc}{E_g}$$

occurs for photons with energies less than the bandgap energy; these photons are not able to effect a transition and are so minimally absorbed that the material is considered transparent to them. For ideal photoconductors and photodiodes operating at wavelengths below the cutoff, $\eta = 1$. However, responsivity for high-energy photons is actually poor as a consequence of the large value of the absorption coefficient at these lower wavelengths. At a penetration depth of x, the transmitted radition intensity, I_v, is reduced from the incident intensity, I_{vo} [24,43].

$$I_v(x) = I_{vo}\exp(-\alpha x)$$

Short wavelength photons are absorbed close to the surface of the semiconductor. These are prone to quickly recombine, which prevents them from contributing to the measured electrical signal.

Although the spectral response of photon-based detectors is narrower than their thermal-based counterparts, photon-based detectors possess a number of advantages. Semiconductor material systems of most consequence to the field of infrared detectors possess direct energy gaps, doping flexibility, high electron mobilities, and low dielectric constants [7]. This endows them with fast response times, high sensitivities, and high signal to noise ratios [1,45].

Photon-based detectors are frequently cooled for better performance. Detectors operating in the MWIR are generally cooled to temperatures between 200 and 77 K,

and it is common to cool those operating in the LWIR to temperatures 77 K or lower. Cooling supresses the thermal generation of carriers, which competes with optical generation processess and obscures the signal. More aggressive cooling is required for LWIR photodetectors, as the smaller energy transitions are more easily triggered by thermal processes. Fulfilling cooling requirements presents an important obstacle to the more widespread adoption of photon-based infrared systems. There is a focus on developing devices having optimal or near-optimal performance at room temperature or, at temperatures greater than 200 K, which are acheivable with thermoelectric coolers. Thermoelectric coolers are lighter-weight and reliable performers with modest power requirements [2,45].

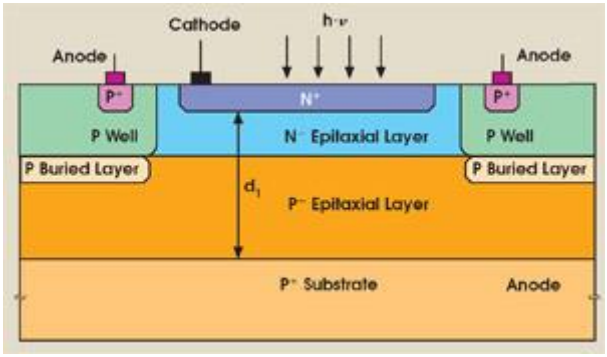

Figure 1.5 Sketch of a Photo Detector [55]

1.6.3 Semiconductor-Based Infrared Photodetectors

A variety of semiconductor materials are used in photon-based infrared photodetectors, with Hg1-xCdxTe and InSb being the most significant to commercial detection systems. While Hg1-xCdxTe is used in both MWIR and LWIR systems, InSb-based systems are exclusive to the MWIR. Other materials, such as extrinsic semiconductors and the lead salts have not been widely adopted for use in the MWIR and LWIR [5].

1.6.4 Mercury Cadmium Telluride (Hg1-xCdxTe)

Hg1-xCdxTe, of the II-VI semiconductor material system, occupies the dominant position in infrared detector systems. The undisputed advantage of using Hg1-xCdxTe is the ability to tune the wavelength sensitivity over an extensive range, from 1 to 30 microns and beyond, during manufacture by adjusting the composition of the ternary. It also experiences notably small changes in lattice constant with changes in composition; the 0.3% change in lattice constant between HgTe and CdTe permits layered and graded-gap structures to be grown as high-quality crystals [2,5,7].

HgCdTe has the direct energy gap, ability to obtain both low and high carrier concentrations, high mobility of electrons and low dielectric constant, HgCdTe is the most widely used variable gap semiconductor material for infrared photodetectors design at present. The extremely small change of lattice constant with composition makes it possible to grow high quality layers and heterostructures. HgCdTe can be used for detectors operated at various modes (photoconductors, photodiodes and MIS detectors), and can be optimized for operation at the extremely wide range of the IR spectrum (from visible region to 30 μm) and at temperatures ranging from that of liquid helium to room temperature.

The manufacturability of Hg1-xCdxTe is a significant issue. Infrared photodetectors fabricated from Hg1-xCdxTe exhibit quantum efficiencies of 50-60 percent without anti-reflective coatings and 70-80 percent with them.

1.6.5 Indium Arsenide Antimonide (InAs1-xSbx)

InAs and InSb, which are both narrow-bandgap binaries of the III-V semiconductor family with similar physical properties, are common MWIR photodetector materials. InSb is the more prevalent as it has a smaller bandgap, 0.22 e_v [32] and a cutoff

wavelength of 5.6 μm, which is better suited to cover the whole 3 to 5 μm wavelength range of the MWIR atmospheric transmission window. InAs possesses a larger bandgap of 0.35 e_v and a consequently shorter cutoff wavelength of 3.6 μm [32]. $InAs_{0.4Sb0.6}$ with a cutoff wavelength of 7.0 μm has been demonstrated. An infrared detector composed of $InAs_{0.1}Sb_{0.9}$ has the potential for 77 K operation at 9.0 μm, which is a cutoff wavelength no other III-V semiconductor can match [55,56].

InSb photodetectors may be photovoltaic or photoconductive, and both monolithic and hybrid arrays have been produced. Hybridized arrays are common; producing monolithic arrays results in detectors having shorter cutoff wavelengths than when they are manufactured separately as well as nonlinearities in the CMOS readout.[2] While free carrier absorption is reduced when the back surfaces of the detector arrays are thinned to 100 microns, they are frequently polished to a 10 micron thickness to achieve higher quantum efficiency [5,7]. The diffusion length of minority carriers in n-type InSb is approximately 30 microns at 80 K, [57] and detector arrays with thicker substrates suffer from a loss of resolution and reduced responsivity [2].

InAs1-xSbx has attracted interest as it can potentially produce detectors operating out to 9 microns, but the challenge of fabricating high-quality material is substantial. The lack of substrates with suitable lattice constants is a key issue; devices grown from alloys closely lattice matched to and grown on GaSb substrates perform best. This material must be passivated to suppress the otherwise high levels of surface leakage current, and the higher levels of generation current, arising from an increased dislocation density in the strained material, is significant. To date, $InAs_{0.91}Sb_{0.09}$ photodetectors have seen acceptance in optical fiber communication systems operating in the 2-4 micron wavelength range [2,7].

1.6.6 Schottky Barrier Photodiodes and the Silicides

Schottky barrier photodiodes have been under sustained development as alternatives to p-n junction photodiodes. They consist of a thin film, which is on the order of 10-20 Angstroms thick and contains heavy metal atoms, in contact with a semiconductor crystal. Palladium, platinum, and iridium are popular dopants, with cutoff wavelengths of 3μm, 5μm, and 10 μm, respectively. Rectification creates a potential barrier between the metal and the doped silicate layers. Incident signal photons are absorbed in the metal-containing film, and those possessing enough energy excite majority carriers over the potential barrier. Majority carriers are typically the carriers of signal current. Carriers may also tunnel through the barrier, and carrier recombination may occur in the space charge and neutral regions. [24,43] Platinum silicide Schottky barriers have enjoyed considerable commercial interest.[2]

Schottky barrier photodiodes have a number of advantages as compared with p-n junction photodiodes. The manufacturing process for the former is notably less complex, they are not subject to diffusion processes at high temperatures, and they have faster response times that allow higher frequency operation. [7] Forward biasing a Schottky barrier photodiode based on an n-type semiconductor crystal injects electrons into the metal-containing film. [24,43] There, collisions between carriers result in thermalization occurring on a time scale of approximately 10-14 seconds. Forward biasing a p-n junction photodiode injects carriers that must instead dissipate through recombination, and minority carrier recombination lifetimes are typically on the order of 0.5 microseconds. The difference in lifetimes results in Schottky barrier photodiodes having the potential for higher frequency operation [7].

Schottky barriers are well suited to applications in which high resolution is required, the background radiation is high, and cooling to temperatures below 80 K is

acceptable. Material uniformity is excellent. Uncorrected uniformity is better than 99 percent for Pt:Si, which allows for the fabrication of large arrays. Arrays of Pt:Si devices with 1040 x 1040 pixels are available. These detectors must be cooled to temperatures below those required by p-n photodiodes and other detectors, due to the necessity of quelling the thermal emission of carriers over the barrier. However, once appropriately cooled, typically to 77 K, the sensitivity of Schottky barrier photodetectors is largely independent of temperature, which is a noted advantage over other types of photon detectors. [2, 7] Sensitivity is low, with scattering mechanisms interfering with the transport of photogenerated carriers. Quantum efficiencies are 4 percent and 0.5 percent for Pt:Si at 2.5μm and 4μm, respectively [2].

1.6.7 Photoconductors

Photoconductors are essentially optically variable resistors, in which conductivity increases when absorbed photons create free carriers. [19, 24, 43] In the case of intrinsic semiconductor material, the cutoff wavelength of the absorbed photons is determined by the bandgap energy. For extrinsic material, it is the difference between the energy of the donor state and the band edge. Photoconductors are structurally simple photodetectors, consisting of a width of semiconductor material sandwiched between two ohmic contacts.

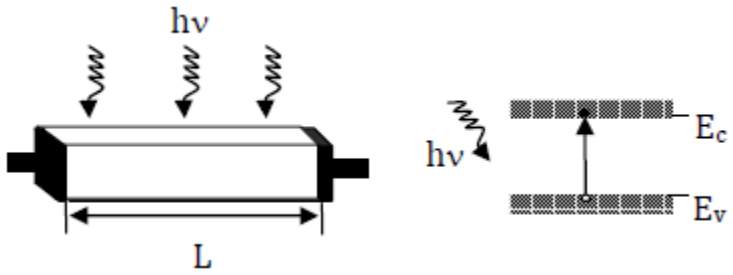

Figure 1.6 Sketch of a Photoconductor[56]

The physical structure is illustrated at left. The schematic at right shows electron-hole

pair generation across the bandgap. E_c is the energy at the bottom of the conduction band and E_v is the energy at the top of the valence band.

During operation, an electric field is applied across the contacts. A current always flows in these devices, due to the lack of barriers and the sustained voltage bias, but the magnitude of the current increases in the presence of a signal. The conductivity is expressed as

$$\sigma = q(\mu_n n + \mu_p p)$$

where q is the charge on the carrier, μn and μp are the electron and hole mobilities, and n and p are the electron and hole densities.

Performance may be quantified in terms of quantum efficiency, gain, response time, and detectivity. The internal quantum efficiency approaches unity, as an absorbed photon nearly always increases the conductivity. The external quantum efficiency can exceed 0.9 when the illuminated surface of the detector is coated with an anti-reflection coating. The gain,

$$G = \frac{I_p}{I_{ph}} = \frac{\tau}{t_r} = \frac{\tau}{L/v_d}$$

where L is the length of the semiconductor and v_d is the drift velocity, is the ratio of the carrier lifetime, τ, and the carrier transit time, t_r, as well as the ratio of the measured photocurrent, I_p, to the primary photocurrent,

$$I_{ph} = q\left(\eta \frac{P_{opt}}{h\nu}\right)$$

The carrier lifetime is a critical parameter to both the gain, which may range from 1 to 10^6, and the response time, which varies from 10^{-3} to 10^{-8} seconds and is longer than that of photovoltaic photodetectors [24]. A benefit of gain includes lessened

dependence on low-noise preamplifiers. However, a longer response time can be a liability; photoconductive photodetectors are limited to lower frequency operation than photovoltaic photodetectors [2,7].

The primary internal noise sources in photoconductive photodetectors are Johnson-Nyquist noise noise, generation-recombination noise, and 1/f noise, for which there is no exact analytical model [19]. Both generation and recombination processes are active in photoconductive photodetectors, while only generation processes are significant in the Barrier photodetector and the p-n junction photodiode. As a consequence, photoconductive photodetectors are constrained to have at least 2 times more noise than photodetectors, in which only the generation process contributes significant noise [19,26]. There are a variety of expressions for generation-recombination noise in photoconductive detectors; each reflects different compositional and operational characteristics.

The advantages of photoconductive photodetectors include high gain and ease of manufacture. This is particularly true of those based on extrinsic silicon and germanium. In the HgCdTe material system photovoltaic photodetectors, with microwatt power dissipation, are generally preferred over the photoconductive, with milliwatt power dissipation. Arrays of extrinsic silicon photoconductive photodetectors are modest in size, usually not larger than 128 x 128, highly sensitive, typically useful into the LWIR, and require cooling to temperatures in the neighborhood of 20 K to reduce dark current to acceptable levels. HgCdTe based photoconductive photodetectors are either operated singly or as groupings of a few elements [2]. Photoconductive photodetectors are not considered significant competitors to the p-n junction photodiode and Barrier photodetector.

1.6.8 p-n Junction Photodiodes

The p-n junction photodiode incorporates a barrier to the flow of majority carriers absent from the photoconductive detector. A p-n junction is formed at the interface of p-type and n-type materials. Diffusion of majority charge carriers across the metallurgical junction creates space charge regions surrounding the junction that are depleted of free charge carriers. This diffusion continues until the electric field arising from the exposed and fixed ions is sufficiently large to discourage the further net migration of the majority charge carriers. In thermal equilibrium, the Fermi energy, Ef, is uniform throughout the device. In the absence of an externally applied field and under steady-state conditions, the built-in potential barrier, Vbi, is used to define the difference between the intrinsic Fermi energies in the n-type and p-type regions.43

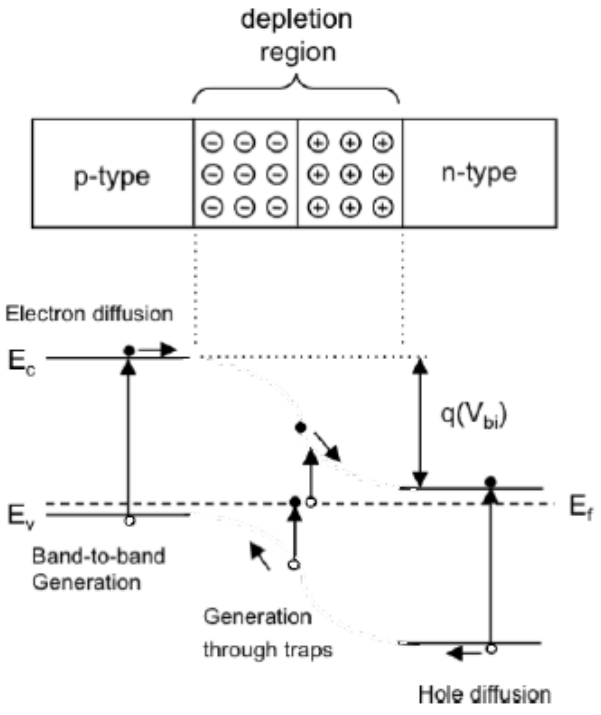

Figure 1.7 Sketch of a p-n junction[17]

Top: The space charge region exists at the interface of p-type and n-type materials. Bottom: Energy diagram of a p-n junction showing Auger (band-to-band) and SRH

generation (trap-assisted) processes. Direction of free carrier diffusion is indicated.

The majority of photogenerated carriers in MWIR photodiodes are produced in the material adjoining the depletion region, rather than in the depletion region itself. Photoexcitation occurring across the bandgap is the preferred process. Arranging for the majority of the absorption to occur in the p-type region is typical, as electrons have a higher mobility than holes. [19] Carriers generated within a diffusion length may diffuse into the space-charge region, where the electric field selectively sweeps the minority carriers through the depletion region. Gain is taken to be unity, except in the case of avalanche photodiodes. Photodiodes may be operated under a negative voltage bias, in the photoconductive mode, or with no voltage bias, in the photovoltaic mode. [24,28]

Dark current in infrared, narrow-bandgap, semiconductor-based photodiodes arises through mechanisms including band-to-band generation (diffusion current), generation through trap states (SRH generation current), Johnson-Nyquist noise, band-to-band tunneling across the depletion region, trap-assisted tunneling through the depletion region, and surface leakage.[19] In the following, only diffusion currents, SRH generation currents, and Johnson-Nyquist noise are treated.

The shot noise model describes the intrinsic noise in infrared photodiodes [19]. When operating in the low-frequency regime, the mean square noise current is

$$\bar{I}_n^2 = 2q\left(I_{sat} \exp\left(\frac{qV}{kT}\right) + I_{sat} \right)\Delta f,$$

where Isat is the saturation current and V is the applied voltage bias. Under the additional constraints of thermal equilibrium, no applied voltage, and no incident radiation, the mean square noise current consists of only Johnson-Nyquist noise,

$$\overline{I_n^2} = \frac{4kT}{R_o}\Delta f.$$

Comparison of above two equations gives the saturation current,

$$I_{sat} = \frac{kT}{qR_o}.$$

Diffusion current in p-n junctions is

$$I_D = I_{sat}\left[\exp\left(\frac{qV}{kT}\right) - 1\right],$$

and SRH generation current, in which W_{dep} is the width of the depletion region and with the assumptions that the Fermi and trap energies coincide and the electron and hole lifetimes are both equal to τ_o, is [19,43]

$$I_{SRH} = \frac{qW_{dep}n_i}{2\tau_o}A.$$

Infrared photodetection systems, particularly those employing large FPAs, frequently incorporate p-n junction photodiodes, which have a number of benefits over photoconductive photodetectors [2]. Stringent noise requirements can be more easily met. Only generation, rather than both generation and recombination, processes are significant in the p-n junction photodiode. This difference alone results in the noise in p-n junction photodiodes being better than that in photoconductive photodetectors by a factor of 2. [19,26] In addition, bias currents in p-n junction photodiodes are low or negligible, which results in lower thermal power dissipation, and coupling to the SiGeut state of a silicon CCD benefits from the naturally high impedance of the

devices. Photodiodes also permit higher-frequency operation, biasing is simpler, and responsivity can be more accurately predicted [2,7].

The preceding discussion of dark current, noise current, and D* does not consider surface leakage current, however the primary contributors to the noise current in narrow-bandgap and cooled p-n junction photodiodes are surface leakage and SRH generation currents. Surface leakage current has an ohmic current-voltage relationship, and it is approximately temperature independent. It is enabled by a uniformly n-type layer that covers the surface of narrow-bandgap semiconductors, regardless of the doping in the bulk. This surface layer arises due to the presence of surface charges. Surface leakage current negatively impacts the performance of the p-n junction photodiode, as charge carriers are able to use surface leakage channels, which run parallel to the depletion region, to bypass the potential barrier. The surfaces of p-n junction based devices are routinely passivated through the application of native oxides or other insulators, to reduce surface leakage current and surface recombination and to protect the devices against undesired environmental effects. [7] Passivation is a time consuming, and hence undesirable process.

While it is possible to mitigate the effects of surface leakage current, SRH current remains a primary source of dark current in cooled photodiodes. The bulk of the SRH current is generated within depletion region, and, as seen in Equation (1.6.10), the magnitude is proportional to both the volume of the depletion region and, through the presence of n_i, the generation rate, G_{SRH}. The key to minimizing SRH current is removing the Fermi level from the middle of the bandgap. The Fermi level may be moved from the middle of the bandgap by designing a photodetector composed of n-type or p-type material and without a depletion region. The Barrier detector, discussed in the next section, is designed to suppress SRH current by displacing the Fermi level

from the middle of the bandgap.6

1.6.9 The Barrier Photodetector

The InAs / AlAsSb Barrier photodetector is shown in Figure 1.8 as a representative of the class of Barrier photodetectors. [6] The name of the Barrier photodetector class derives from the n-type absorption layer, the Barrier layer, and the n-type contact layer. Signal photons interacting with the absorption layer result in band-to-band excitations, and signal current is generated when the resulting holes travel to the contact.

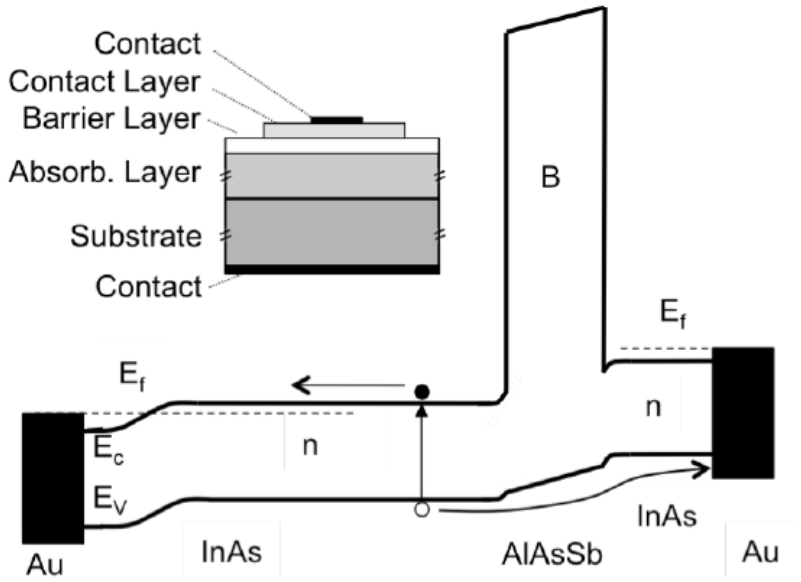

Figure 1.8 Sketch of the voltage-biased Barrier photodetector[23]

The Barrier photodetector design stipulates that there be no energy discontinuity in the valence band, and consequently no barrier to the free flow of minority carrier holes. However, the intentionally large conduction band energy discontinuity, which is much larger than kT, blocks the flow of the majority carrier electrons. In the InAs-based Barrier photodetector, both the zero valence band and the large conduction band energy discontinuities may be achieved by an AlAsxSb1-x barrier layer with a specific composition, x, which is found to be $0.14 < x < 0.17$. A pixel is defined by

etching through the contact layer; the barrier layer acts as an etch stop. Gold metal contacts are deposited on top of the contact layer. The Barrier photodetector operates under a voltage bias, and the bias applied to the device shown in Figure 1.8 is referred to as a reverse bias.

The fabricated device structure is shown at the upper left, and the energy diagram is beneath. The contacts are gold, the substrate, absorption, and contact layers are n-type InAs, and the barrier layer is AlAsSb. In the energy diagram, the contact layer is located to the right of the barrier layer.

The design of the Barrier photodetector suppresses SRH generation current and reduces surface leakage current to negligible levels. [6] Nowhere does the Fermi energy coincide with the middle of the bandgap, which significantly reduces the SRH generation rate. Surface leakage current is essentially eliminated by the inclusion of the wide bandgap barrier layer.

1.7 Goal of This Thesis

The Goal of this thesis is to investigate the CMOS compatible MDIR structure based on avalanche and heterjunction mechanism.

Chapter 2: introduce Dark current and Barrier Infrared Photodiode.

Chapter 3 compares the simulation results of the designed SiGe/Si HIP SAM MDIR APD

Chapter 4 provides the conclusions

Chapter 2 Dark Current and IR Photodiode Structure

2.1 Analysis of the Dark Current in Photodetector

In a photon detector, the infrared radiation is absorbed by a quantum process, thus solving the problems associated with thermal detectors. However, photon detectors have not general been suitable for use at room temperature; this issue is explained below. The infrared radiation emitted by the human body at 36 C has a wavelength range of 3–25 μm, with a peak at 10 μm. In the case of an ideal diode, the output current IL of the photodiode to an external resistance under infrared irradiation is expressed as follows:

$$I_{\mathrm{L}} = I_{\mathrm{ph}} - I_{\mathrm{d}},$$
$$I_{\mathrm{d}} = A I_0 \left\{ \exp\left(\frac{qV}{kT}\right) - 1 \right\},$$

where Iph is the photocurrent generated by exposure to infrared irradiation, Id is the diffusion current, k is the Boltzmann constant, T is the absolute temperature, q is the electron charge, V is the bias voltage, and A is the infrared irradiation absorption area. The saturation current density I0 is given by

$$I_0 = \sqrt{kT} n_{\mathrm{i}}^2 \sqrt{q} \left\{ \frac{1}{p_{\mathrm{p0}}} \left(\frac{\mu_{\mathrm{e}}}{\tau_{\mathrm{e}}}\right)^{1/2} + \frac{1}{n_{\mathrm{n0}}} \left(\frac{\mu_{\mathrm{h}}}{\tau_{\mathrm{h}}}\right)^{1/2} \right\},$$

where ni is the intrinsic carrier concentration, pp0 and nn0 are the hole and electron majority carrier concentrations, τe and τh are the hole and electron mobilities, and μe and μh are the electron and hole lifetimes of the p- and n-type regions, respectively.

This shows that the diffusion current varies with temperature as n_i^2. Because the bandgap of infrared material is small, an intrinsic carrier density of 1.5×10^{16} cm^3 is

generated even at room temperature. Therefore, because the diffusion current is high at room temperature, the output current is very small if the device is not cooled.

The resistance under zero bias (R_o) is affected by the saturation current density, and R_o is expressed as follows:

$$R_0 = \frac{kT}{qI_0A}.$$

Therefore, a large R_o value indicates that the device is a good photodiode with a small diffusion current. The R_oA product is frequently encountered as a figure of merit for a photodiode. However, the photocurrent I_{ph} can be raised by a photodiode structure that absorbs the infrared rays efficiently. A rise in I_{ph} directly increases the output current I_L.

Therefore, the important considerations when creating an infrared photon detector for use at high temperature are as follows:

1. Suppressing the diffusion current while increasing the resistance R_o of the Photodiode
2. Increasing both the infrared incidence efficiency and the photocurrent I_{ph}.

2.2 New Materials and new structures needed for IR Photodiode

Although HgCdTe is the main IR photodiode material, there are motivations to replace HgCdTe because of the technological problems with this material; one of them is a weak HgTe bond; which results in bulk, surface and interface instabilities. Uniformity and yield are still issues of HgCdTe, especially in the LWIR spectral range. Nevertheless, HgCdTe remains the leading semiconductor for IR detectors.

Recently, there has been a considerable progress towards the IR materials' development and device design innovations. In particular, significant advances have been made during the last two decades in the bandgap engineering of various

compound semiconductors that has led to the new detector architectures. New emerging strategies include barrier structures such as Barrier detector, low dimensional solids type 2 super lattice [T2SL] with lower generation/recombination leakage mechanisms, photon trapping detectors and multistage/cascade infrared devices.

2.3 Concept of barrier infrared detector

Historically, the first barrier detector was proposed by A.M. White in 1983 as a high impedance photoconductor [16]. It postulates an n type heterostructure with a narrow gap absorber region coupled to a thin wide bandgap layer, followed by a narrow bandgap contact region. The concept assumes almost zero valence band offset approximation throughout the heterostructure, what allows for a flow of only minority carriers in a photoconductor. Little or no valence band offset was difficult to realize using standard infrared detector materials such as InSb and HgCdTe. Situation has changed dramatically in the middle of the first decade of 21 century after introducing of III-V material detector family and when the first high performance detectors and FPAs were demonstrated [3, 5]. Introducing of unipolar barriers in various designs based on T2SLs drastically changed the architecture of infrared detectors [6]. In general, unipolar barriers are used to implement the barrier detector architecture for increasing the collection efficiency of photo generated carriers and reducing dark current generation without inhibiting photocurrent flow. [6]

The term “unipolar barrier” was coined to describe a barrier that can block one carrier type (electron or hole) but allows for the unimpeded flow the other carrier type. Between different types of barrier detectors the most popular is Barrier detector shown in Figure 2.1. The n-type semiconductor on one side of the barrier constitutes a contact layer for biasing the device; while the n-type narrow bandgap semiconductor

on the other side of the barrier is a photon absorbing layer whose thickness should be comparable to the absorption length of light in the device, typically several microns. The same doping type in the barrier and active layers is key to maintaining low, diffusion limited dark current.

The barrier must be nearly lattice matched to the surrounding material and have a zero offset in the one band and a large offset in the other band. It should be located near the minority carrier collector and away from the region of optical absorption. Such barrier arrangement allows photo generated holes to flow to the contact (cathode) while majority carrier dark current, reinjected photocurrent and surface current are blocked So, the Barrier detector is designed to reduce dark current (associated with SRH processes) and noise without impending photocurrent (signal). In particular, the barrier serves to reduce surface leakage current.

The makeups of the various current components and barrier blocking in Barrier detector are shown in the bottom right side of Figure 2.1.

The Barrier detector is essentially a photoconductor with unity gain due to the absence of majority carrier flow; and in this respect Barrier detector is similar to a photodiode: the junction is replaced by an electron blocking unipolar barrier (B), and that the p type contact is replaced by an n type contact. It can be stated, that the Barrier design is a hybrid between photoconductor and photodiode. Figure 2.2 shows a typical Arrhenius plot of the dark current in a conventional diode and in Barrier detector. The diffusion current typically varies as $T^{3\exp(-Ego/KT)}$, where E_{g0} is the band gap extrapolated to zero temperature, T is the temperature, and k is the Boltzman's constant. The generation-recombination current varies as $T^{3/2\exp(-Ego/KT)}$ and is dominant by the generation of electrons and holes by SRH traps in the depletion region.

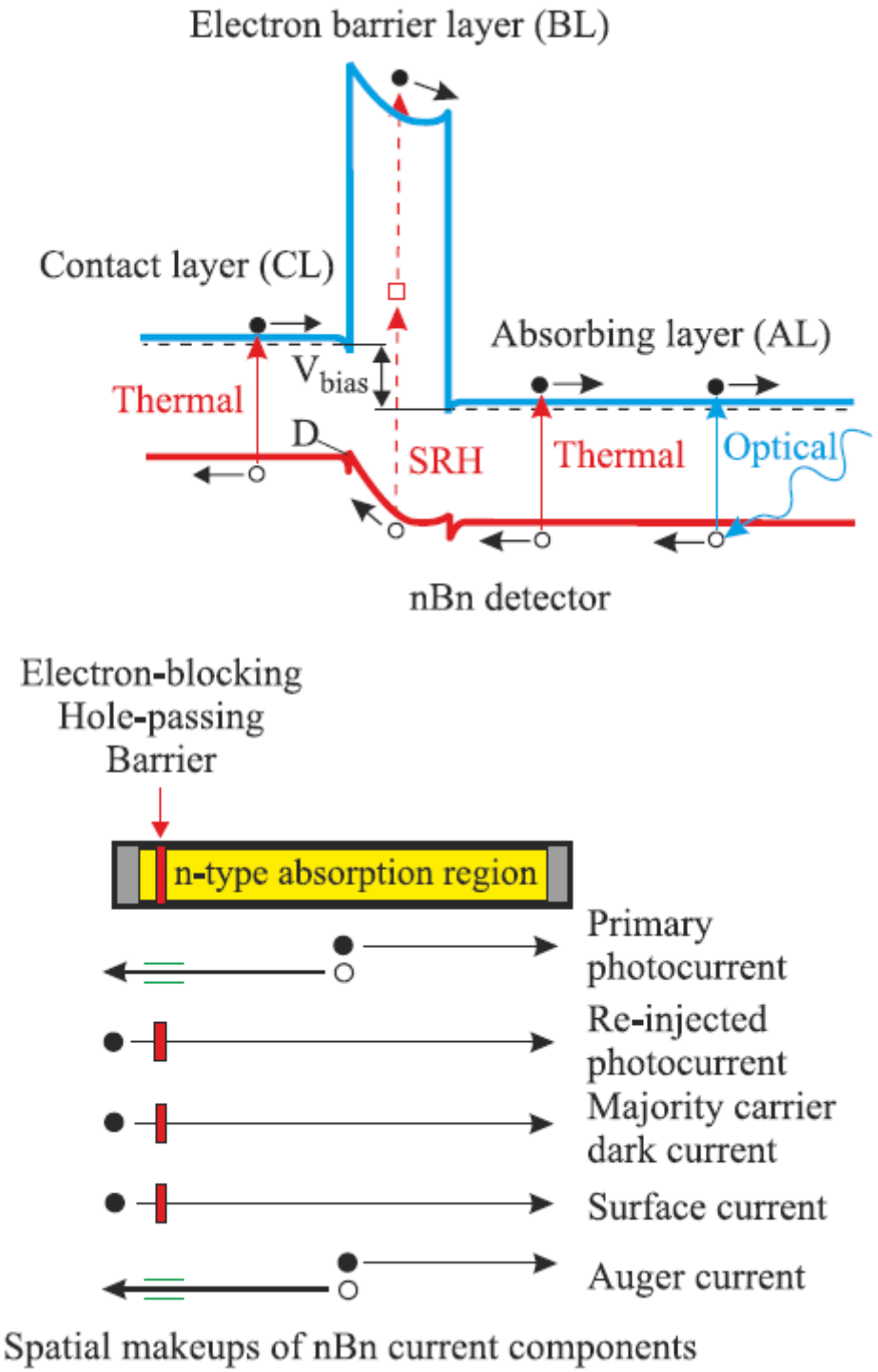

Figure 2.1 Barrier Photodetector[38]

Because in Barrier detector there is no depletion region, the generation-recombination contribution to the dark current from the photon-absorbing layer is totally suppressed. The lower portion of Arrhenius plot for the standard photodiode has a slope that is

roughly half that of the upper portion. The solid line (Barrier) is an extension of the high temperature diffusion limited region to temperatures below T_c. T_c is defined as the crossover temperature at which the diffusion and generation-recombination currents are equal. In a low temperature region, Barrier detector offers two important advantages. First, it exhibits a higher signal to noise ratio than a conventional diode operating at the same temperature. Second, it operates at a higher temperature than a conventional diode with the same dark current. This is depicted by a horizontal green dashed line in Figure 2.2.

Wide family of barrier detectors has been considered by Klipstein *et al*. [13]. They can be divided in two groups: XB_nn and XB_pp detectors (see Figure 2.3). In the case of the first group, all have the same n-type Bnn structural unit, but used different contact layers (X), where either the doping, material, or both are varied. If we take CpBnn and Barrier devices, Cp is the p-type contact made from a different material to the active layer, whereas n is the n-type contact made from the same material. In the case of pBnn structure, the p-n junction can be located at the interface between the heavily doped p-type material and the lower doped barrier, or within the lower barrier itself. The barrier detector family also has p-type members, designated as XB_pp, which are polarity reversed versions of the n-type detectors. The pBp architecture should be employed when the surface conduction of the materials is p-type and must be used a p-type absorbing layer. The last structure can be realized using a p-type InAs/GaSb T2SLs as the absorbing layer [14,15]. So called pMp device consists of two p-doped superlattice active region and a thin M structure with higher energy barrier. The band gap difference between superlattice M-structure falls in the valence band, creating a valence band barrier for the majority holes in a p-type semiconductor.

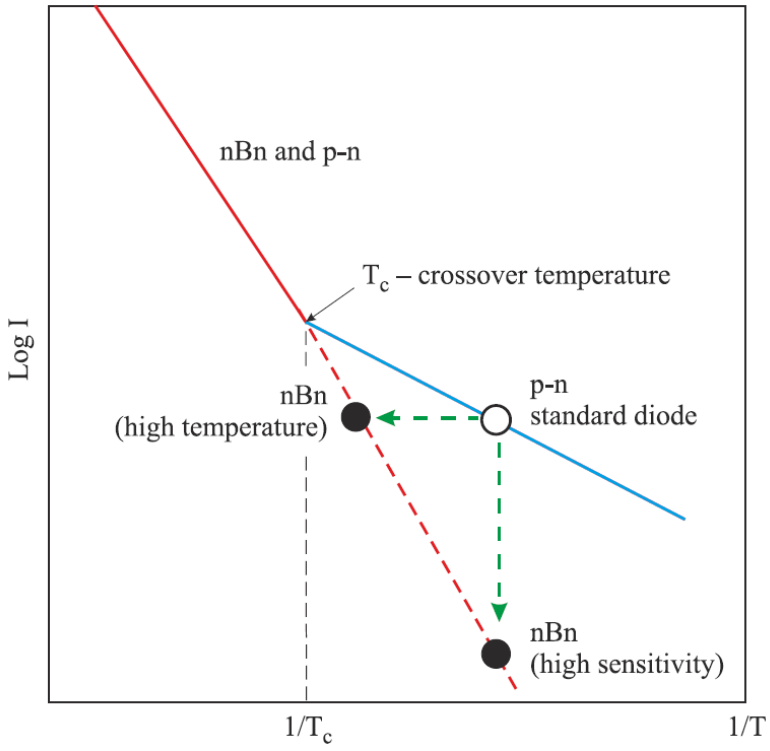

Figure 2.2. Schematic Arrhenius plot of the dark current in a standard diode and in Barrier device[38]

In each case the contact layer (X) is on the left, and infrared radiation is incident onto the active layer on the right. When *X* is composed of the same material as the active layer, both layers have the same symbol (denoting the doping type), otherwise it is denoted as C with the doping type as a subscript. Unipolar barriers can also be inserted into conventional p-n photodiode architecture [7, 16]. There are two possible locations into which a unipolar barrier can be implemented: outside of depletion layer in the p-type layer or near the junction, but at the edge of the n-type absorbing layer (see Figure 2.4). In dependence of barrier placement, different dark current components are filtered. For example, placing the barrier in the p-type layer blocks surface current, but currents due to diffusion, generation-recombination, trap assisted tunneling, and band to band tunneling cannot be blocked. If the barrier is placed in the n-type region, the junction generated currents and surface currents are effectively filtered out. The photocurrent shares the same spatial makeup as the diffusion current, what is shown in Figure 2.4.

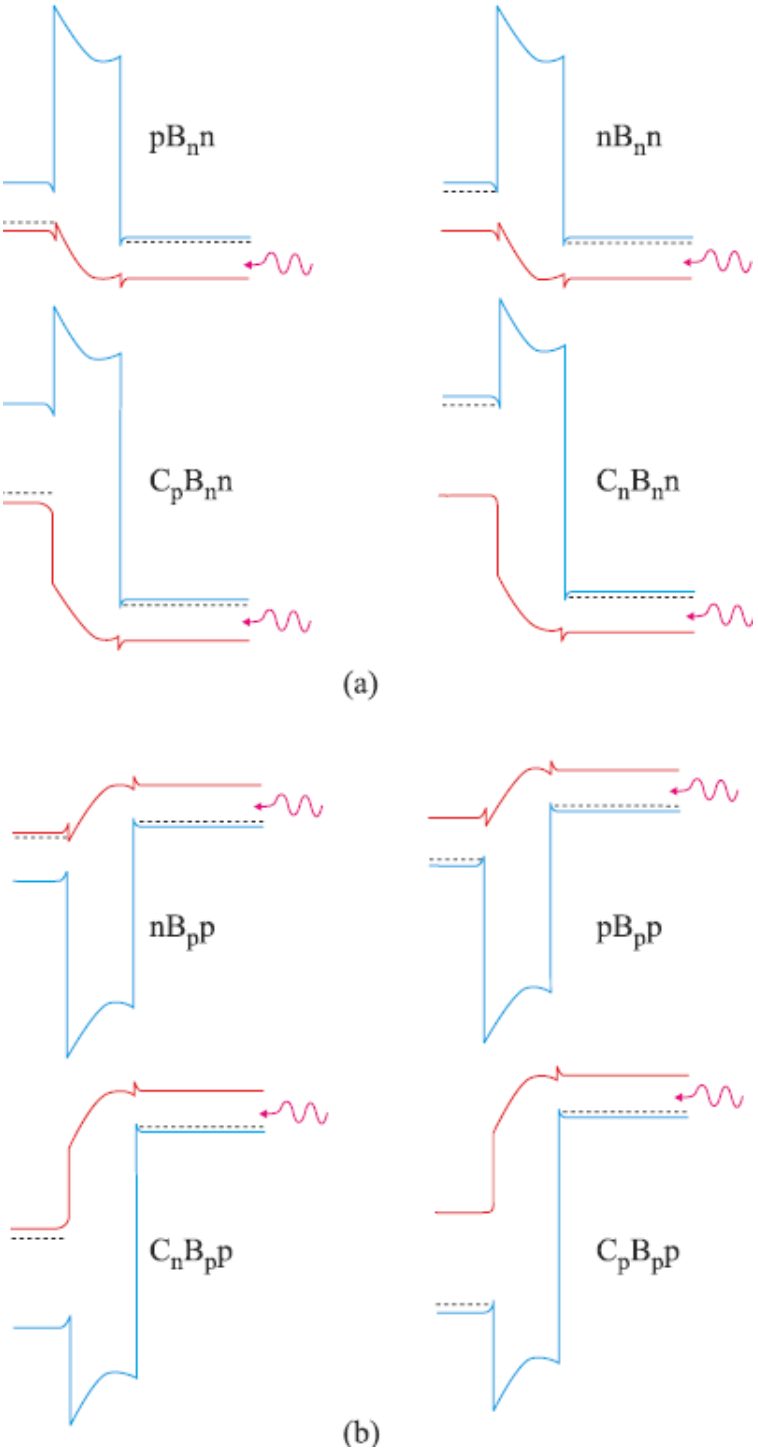

Figure 2.3 Schematic band profile configurations under operating bias for XBnn (a) and XBpp (b) barrier detector families[38]

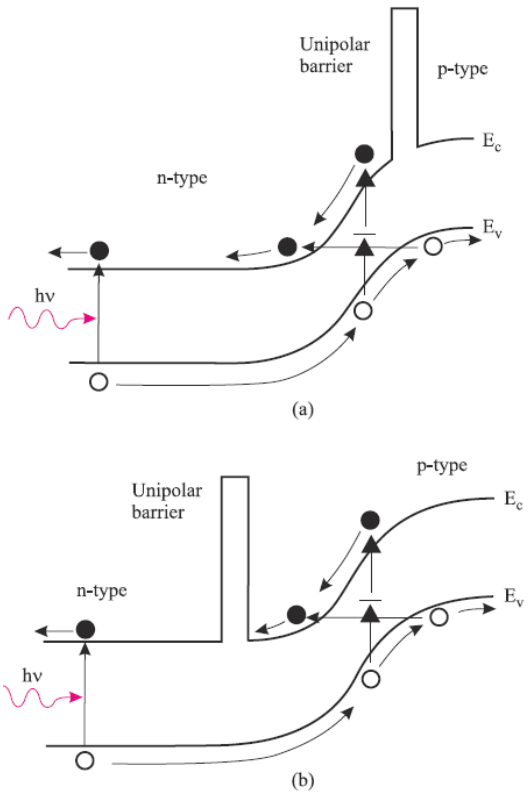

Figure 2.4 p-n photodiode with Barrier[37]

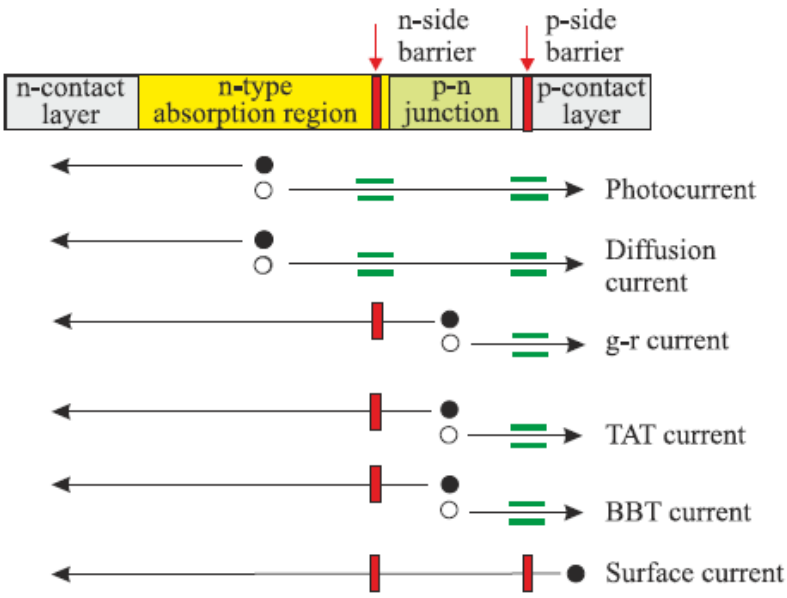

Figure 2.5 The photocurrent shares the same spatial makeup as the diffusion current[33]

2.4 Material considerations for barrier infrared detectors

The barrier detector can be implemented in different semiconductor materials.

Absence of a depletion region offers a way for materials with relatively poor SR lifetimes, such as all III-V compounds, to overcome the disadvantage of large depletion dark currents.

Table 1 physical properties of semiconducting families used in fabrication of infrared photodetectors[43]

	Si	Ge	GaAs	AlAs	InP	InGaAs	AlInAs	InAs	GaSb	AlSb	InSb	HgTe	CdTe
Group	IV	IV	III–V	III–V	III–V	III–V	III–V	III–V	III–V	III–V	III–V	II–VI	II–VI
Lattice constant (Å)/structure	5.431 (D)	5.658 (D)	5.653 (ZB)	5.661 (ZB)	5.870 (ZB)	5.870 (ZB)	5.870 (ZB)	6.058 (ZB)	6.096 (ZB)	6.136 (ZB)	6.479 (ZB)	6.453 (ZB)	6.476 (ZB)
Bulk moduls (Gpa)	98	75	75	74	71	69	66	58	56	55	47	43	42
Band gap (eV)	1.124 (id)	0.660 (id)	1.426 (d)	2.153 (id)	1.350 (d)	0.735 (d)		0.354 (d)	0.730 (d)	1.615 (id)	0.175 (d)	0.141 (d)	1.475 (d)
Electron effective mass	0.26	0.39	0.067	0.29	0.077	0.041		0.024	0.042	0.14	0.014	0.028	0.090
Hole effective mass	0.19	0.12	0.082(L) 0.45(H)	0.11(L) 0.40(H)	0.12(L) 0.55(H)	0.05(L) 0.60(H)		0.025(L) 0.37(H)	0.4	0.98	0.018(L) 0.4(H)	0.40	0.66
Electron mobility (cm^2/Vs)	1450	3900	8500	294	5400	13800		3×10^4	5000	200	8×10^4	26500	1050
Hole mobility (cm^2/Vs)	505	1900	400	105	180			500	880	420	800	320	104
Electron saturation velocity (10^7 cm/s)	1.0	0.70	1.0	0.85	1.0			4.0			4.0		
Thermal cond. (W/cmK)	1.31	0.31	0.5		0.7			0.27	0.4	0.7	0.15		0.06
Relative dielectric constant	11.9	16.0	12.8	10.0	12.5			15.1	15.7	12.0	17.9	21	10.2
Substrate	Si,Ge		GaAs		InP			InAs,GaSb			InSb	CdZnTe,GaAs,Si	
MW/LW detection mechanism	Heterojunction internal photoemission		QWIP,QDIP		QWIP			Bulk (MW) Superllatice (MW/LW) Band-to-band (B-B)			Bulk B-to-B	Bulk Band-to-band	

D – diamond, ZB – zincblende, id – indirect, d – direct, L – light hole, H – heavy hole

The main requirement which must be met to construct the barrier detector structure is "zero" band offset in a proper band depending on carrier type which is to be blocked. Material systems where a large conduction band offset is not realizable, the pBn architecture may be preferable. The traditional Barrier structure requires bias to operate. Once zero bias operation is crucial, again pBn architecture may be used [21]. The large band offset requirement in one band and zero offset in the other is not the only one requirement to fabricate a barrier detector; the lattice matching between surrounding materials is also significant. Table 1 presents some physical properties of semiconducting families used in fabrication of infrared photodetectors. All compounds have diamond (D) or zincblende (ZB) crystal structure. Moving across the table from the left to the right, there is a trend in change of chemical bond from the covalent group IV-semiconductors to more ionic II-VI semiconductors with increasing

of the lattice constant. The chemical bonds become weaker and the materials become softer what is reflected by the values of the bulk. The materials with larger contribution of covalent bound are more mechanically robust, which leads to better manufacturability. This is evidenced in the dominant position of silicon in electronic materials and GaAs in optoelectronic ones. On the other hand, the band gap energy of semiconductors on the right side of the table tends to have smaller values. Due to their direct band gap structure, strong band to band absorption leading to high quantum efficiency is observed.

The most promising materials for barrier detector structures are InAs(InAsSb)/B-AlAsSb and InAs/GaSb T2SLs due to nearly zero V_{BO} with respect to AlAsSb barriers. The InAsSb ternary alloy has a fairly weak dependence of the band edge on composition and is used in MWIR region. It was shown that by decreasing the valence band offset in InAsSb Barrier devices, signal to noise ratio increases [18]. The InAs/GaSb T2SLs can be used as mid or long wave length infrared absorber. In particular, the ability to tune the positions of the conduction band and valence band edges independently in the T2SL is especially helpful in the design of unipolar devices. This material system is in an early stage of development. Problems exist in material growth, processing, substrate preparation, and device passivation. Optimization of SL growth is a tradeoff between interface roughness, with smoother interfaces at higher temperature, and residual background carrier concentrations, which are minimized on the low end of this range.

Chapter 3 The Designed MDIR Photodiode

3.1 SiGe/Si HIP Concept

One type of internal photoemission detector, which incorporates a degenerately doped semiconductor electrode in place of silicide, was proposed as a variant to the basic Schottky-barrier detector by Shepherd et al. [5] in 1971. This concept was first implemented in 1990 by workers at the Jet Propulsion Laboratory, who fabricated Si-based heterojunction detectors consisting of a heavily doped p-GeSi as shown in Figure 3.1, epitaxial layer on a single-crystal p-Si substrate. These devices were sensitive out to at least 10 μm. The operating principle of the GeSi/Si HIP detectors is illustrated in Fig3.2. Infrared photons with energies less than the bandgap of Si are transmitted through the Si substrate into the p+-SiGe layer, where a fraction is absorbed by free holes. A fraction of the photoexcited holes that have energies greater than the barrier height Ψ are emitted into the Si and collected to produce the detector photocurrent. The magnitude of Ψ (which is approximately determined by the valence-band offset ΔE_v), and therefore the detector cut off wavelength, can be tailored by varying the composition of the SiGe layer.

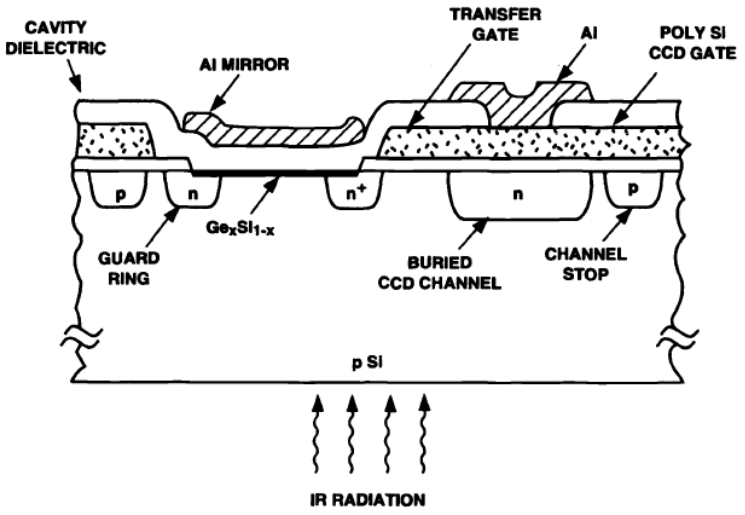

Figure 3.1 Schottky-barrier detector

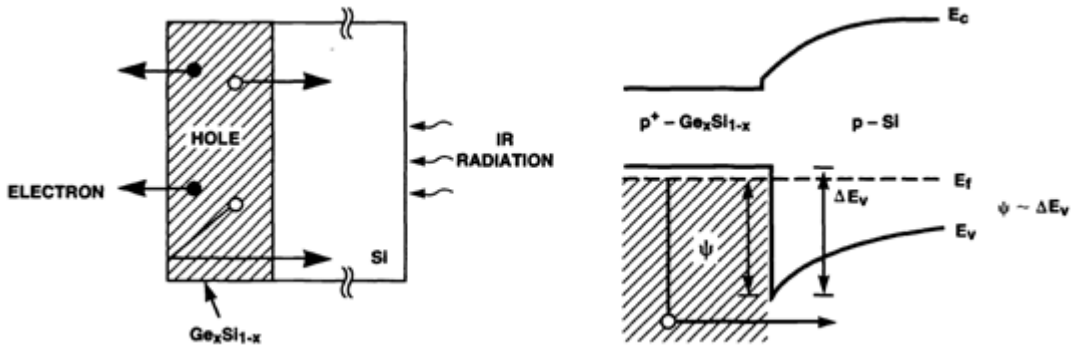

Figure 3.2 The operating principle of SiGe/Siheterojunction detectors

The cutoff wavelength λ_c of the HIP detector is determined by the heterojunction barrier Ψ**,** and is given by

$$\lambda_c = 1.24 / q\psi(eV)$$

The heterojunction barrier Ψ is determined by the valence band offset ΔE_v, between the SiGe alloy layer and the Si substrate, and the Fermi level in the degenerately doped SiGe layer (Figure 3.2), and is given by

$$q\psi = \Delta E_v - (E_v - E_F)$$

The energy band alignment of the SiGe/Si heterostructure has been studied extensively, and the bandgap difference splits approximately 90%/10% between the valence and conduction bands offset *[6]*. The bandgap of commensurately strained The bandgap of commensurately strained SiGe alloys, and correspondingly the SiGe/Si valence band offset AEv, can be tailored by varying the Ge composition. Figure 3.3 shows the SiGe/Si valence band offset ΔE_v and corresponding minimum cutoff wavelengths calculated from the experimental data reported by People ***et*** *al.* [6] for Ge composition of 0.1 to 0.4. The cutoff wavelength of the SiGe/Si HIP detector ***hc,*** can be tailored over a wide IR range; for example, 5 - 22 μm with x ranging from about 0.4 to 0.1. The tailorable cutoff wavelength can be used to optimize the trade-off between the LWIR response and the cooling requirements of the detector.

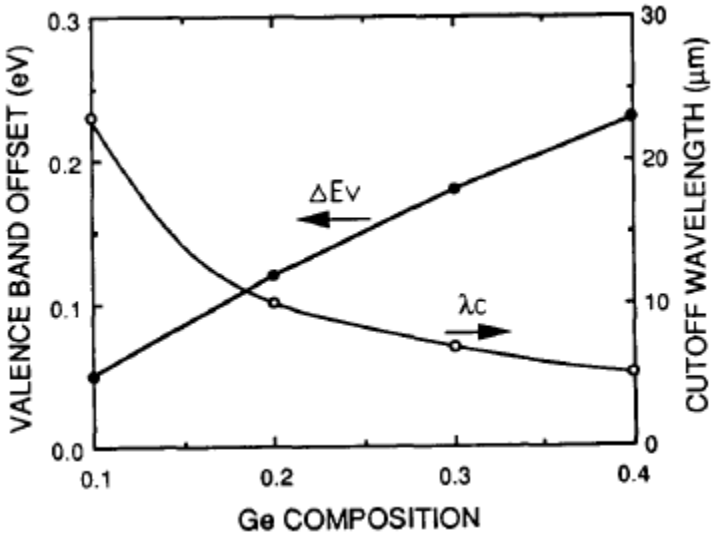

Figure 3.3 Calculated SiGe/Si valence band offsets and corresponding cutoff wavelengths as functions of Ge composition[47]

3.2 MDIR APD Design Merit of this Thesis

Based on previous analysis, the designed MDIR should include the following features:

1 easy for fabrication
2 low internal defects
3 reduced dark current
4 reduced operating temperature
5 reasonable quantum efficiency

Because silicon has the strong bond to bond strength and it also has outstanding low internal defects, silicon is selected as the base material.

Usually the absorption coefficient is high for infrared semiconductor material, such as it can reach few micro meters, which is not efficient for CMOS compatible fabrication; SiGe/Si HIP structure is selected, since its structure has different mechanism to absorb infrared radiation as mention above.

3.3 Separate Absorption Multiplication (SAM) Reach Through APD

For increasing the quantum efficiency of designed MDIR, the avalanche mechanism as shown in Figure 3.4 is included.

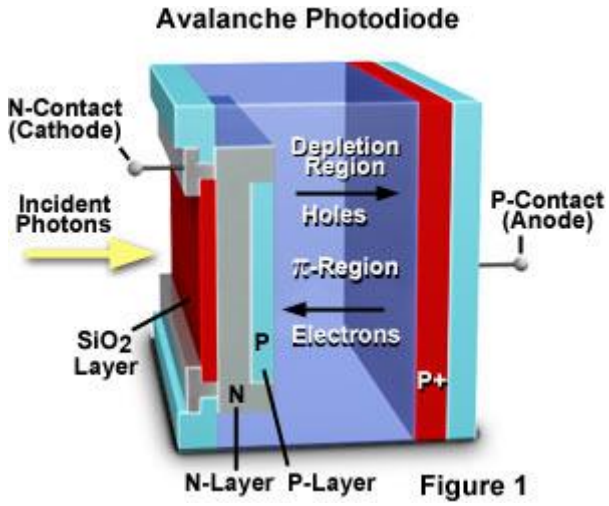

Figure 3.4 structure of avalanche photodiode [57]

Detection in APDs takes advantage of the internal photoelectric effect as well as the phenomenon of avalanche multiplication of carriers in a reverse-biased silicon p-n junction.

Electromagnetic radiation whose energy is at least as great as the energy gap of silicon (E= 1.15 eV) is absorbed in a silicon photodetector structure. The incident photon flux Q decays when it penetrates deep into the semiconductor in accordance with the function $Q(x)= Q\exp(-\alpha x)$, where α is an absorption coefficient for a given wavelength.

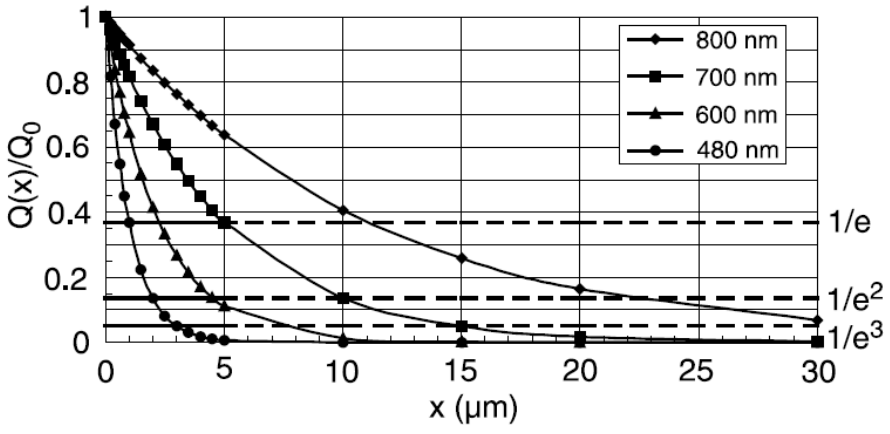

Figure 3.5 Relative distribution of photons in silicon for different wavelengths of radiation [48]

The distance (from the surface) at which the photon flux decreases e-fold – and is equal the reciprocal of absorption coefficient – is called a depth of photon penetration

into the semiconductor. In Figure 3.5, the relative distribution of photons in silicon as the function of the distance from silicon surface for different wavelengths is shown.

The distances (depth of penetration) at which the photon flux is decreasing e-fold, e2-fold, and e3-fold are marked in that figure. As it can be seen, the higher the radiation energy is (shorter wavelength) the smaller the depth of photon penetration becomes. The absorbed flux causes generation of electron-hole pairs in semiconductor. The pairs are separated in a reverse-biased junction of photo-detector structure (see point 3 – design consideration). The effect that consists of generation, transport and recording in the external circuit of optical generated charge carriers is called the internal photoelectric effect and is characterised by an internal quantum efficiency ηi. However, because a part of incident radiation is reflected by a semiconductor surface, the detection process is characterised by external quantum efficiency η_e, and $\eta_e = (1 - R_\lambda)\eta_i$ where R_λ is the reflection index.

In order to obtain the highest sensitivity, the absorption region should be sufficiently thick (most often it is $2/\alpha$), while the reflection index as low as possible.

An avalanche phenomenon takes place if the electric field strength in a p-n junction is higher than strength of so called critical field at which impact ionisation of carriers occurs [44, 45]. In silicon E= 1×10^5 V/cm. The electric field cr in a silicon p-n junction of an avalanche photodiode range from 2 to $5x10^5$ V/cm and cannot exceed the value of 106 V/cm at which the Zener effect happens.

The impact ionisation effect is characterised by the ionisation coefficient – the average number of electron-hole pairs created by one charge carrier (electron or hole) per unit of distance (cm), during its transit in the high electric field.

For most semiconductor materials (except germanium) ionisation coefficients for electrons α and for holes β differ. In Si, ionisation coefficients for electrons α are

much higher than ionisation coefficients for holes β hence an avalanche multiplication factor M_e for electrons is higher, than for holes M_h. The dependence of β/α in silicon, so-called k factor, on the electric field is presented in Figure 3.6.

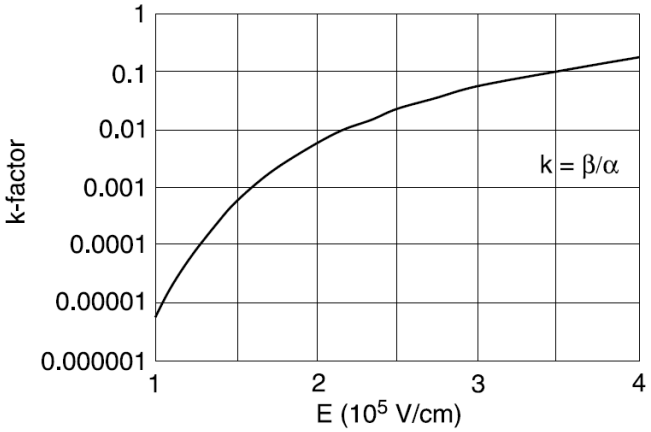

Figure 3.6 Ratio of ionisation coefficients (k-factor) as a function of electric field [47]

The APD should maximize photon absorption only. However the multiplication region should be thin in order to minimize secondary ionizations. These two conflicting requirements are achieved in Separate Absorption Multiplication (SAM) reach Through APD as shown in Figure 3.7. It has been demonstrated that resonantcavity-enhanced separate-absorption-and-multiplication (SAM) avalanche photodiodes (APD's) can achieve high bandwidths and high gain bandwidth products while maintaining good quantum efficiency. Photodiodes with high speed and sensitivity are necessary components in long-haul, high-bit-rate optical communication systems. Avalanche photodiodes (APD's) are preferred for these systems because their internal gain results in higher sensitivity than PIN photodetectors. The requirements for high-performance APD's include high quantum efficiency, high speed, low dark current, a high gain–bandwidth product, and low multiplication noise. Resonant-cavity separate-absorption-and-multiplication (SAM) APD's have been shown to achieve all of these properties [37, 38]. The SAM structure has separate high-field multiplication and absorption regions. Usually this

results in lower dark currents [42]. Another benefit of the SAM APD structure is that only a single type of carrier is injected into the multiplication region, which is a well-known requirement for reducing the multiplication noise that arises from the stochastic nature of the multiplication process [51]. As a result of their excellent performance, SAM APD's have been widely deployed in optical communications systems [43, 45].

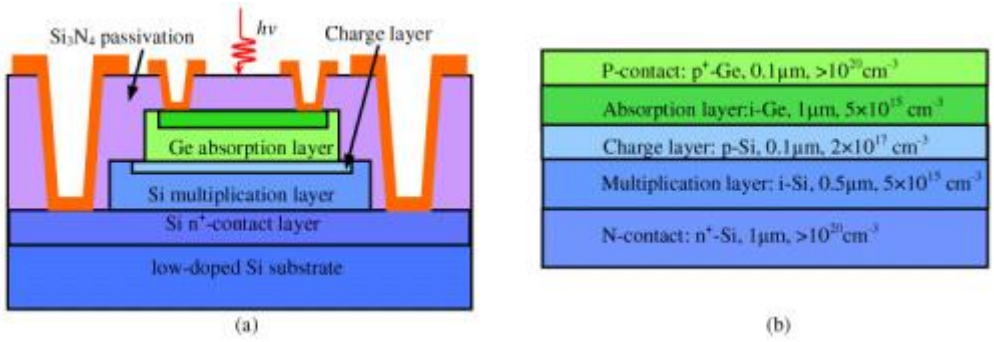

Figure 3.7 Separate Absorption Multiplication (SAM) Reach Through APD [58]

3.4 The designed SiGe/Si HIP MWIR APD

Although SiGe/Si HIP structure was implemented into IR photodiode design decades ago, it is not considered in recent years.

In this design, SiGe/Si HIP is used to detect different wavelengths of infrared. To reduce the dark current in the designed MDIR APD, the band barrier is implemented. The Figure 3.8 and Figure 3.9 show the structures of the designed MDIR APDs. The table below shows the basic data of the designed CMOS SAM APD:

Physical Data of the designed CMOS SAM APD

Thickness	Diameter	Wavelength	Reverse Bias voltage	Operating Temperature
0.8 µm	32 µm	5 µm	0 - 10.5V	25 C

In the design, The generated electrons are swept by electric field to the n-contact, and generated holes travel to the P+ multiplication layer, i.e. nearly pure injection of

photo-generated holes into the gain region is obtained, which gives the most advantageous structure for low-noise operation. An effective active surface area is 32 μm in diameter, above which is coated with an antireflection SiN*x* layer and Al is use as electrode materials.

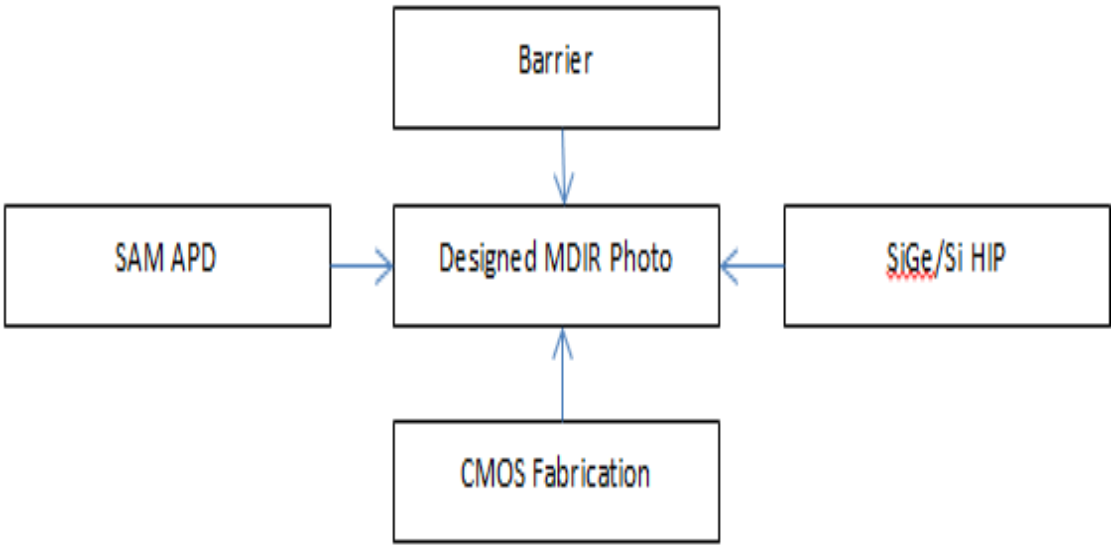

Figure 3.8 the implemented techniques in the designed MDIR photo detector

Based on literature review, the designed structure is the only IR photodiodes utilizing SiGe/Si HIP and SAM avalanche structure in recent years to implement the middle wavelength IR photodiode application.

3.4.1 Photodiode Variables have been investigated

For reducing the dark current, band barrier is implemented in the designed MDIR. Since GaP has 1% lattice mismatch with Silicon and AlAs has the 4% lattice mismatch with Silicon, GaP and AlAs layer were implemented on P+ sides of photodiode. But only the simulation results using AlAs as band barrier are shown since dark current of photodiode using GaP as band barrier and dark current of photodiode without band barrier are at the same level. The reason why AlAs has good dark current surpass prosperity can be explained as: AlAs has high band offset on

both conduction band and valance band of silicon.

Only the substrate thickness of silicon was tuned in simulation for tuning the proper electrical field; the other thickness of each layer was kept as original design for deducing tunnelling current.

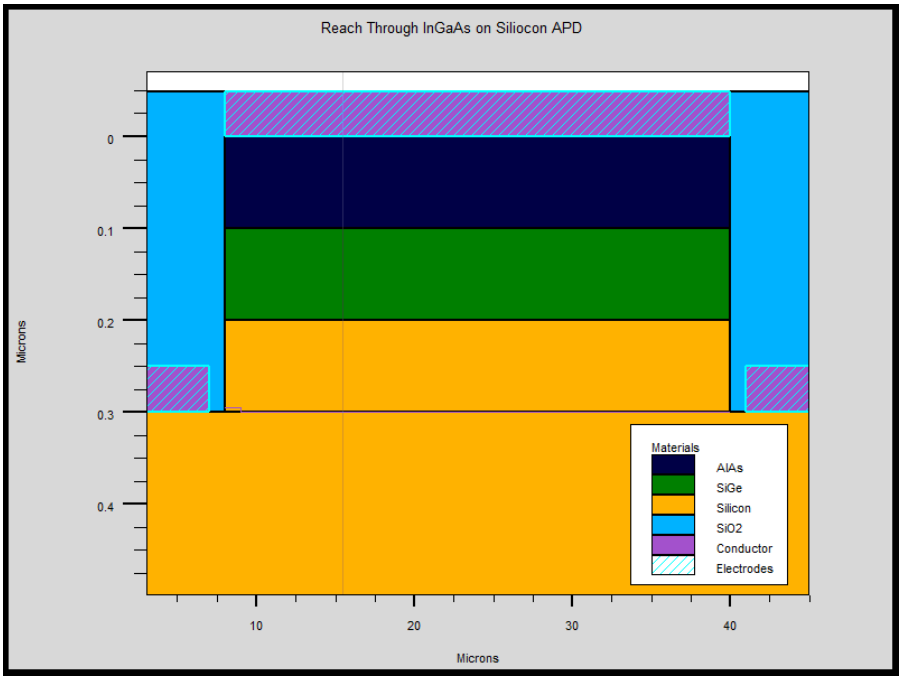

Figure 3.9 structure of the designed CMOS MDIR APD

The designed CMOS SAM APD structure in Detail

Distance µm	Material	Doping (cm^{-3})
-0.05 – 0.1	Al	**None**
0.0 – 0.1	AlAs	P doping at 1 $x10^{11}$
0.1 – 0.2	$Si_{0.8}Ge_{0.2}$(Strained)	P doping at 1 $x10^{18}$
0.2 – 0.25	Si	P doping at 1 $x10^{12}$
0.25 – 0.3	Si	P doping at 1 $x10^{14}$
0.3 - 0.5	Si	N doping at 2 $x10^{17}$

3.5 Simulation results of SiGe/Si HIP MDIR APD

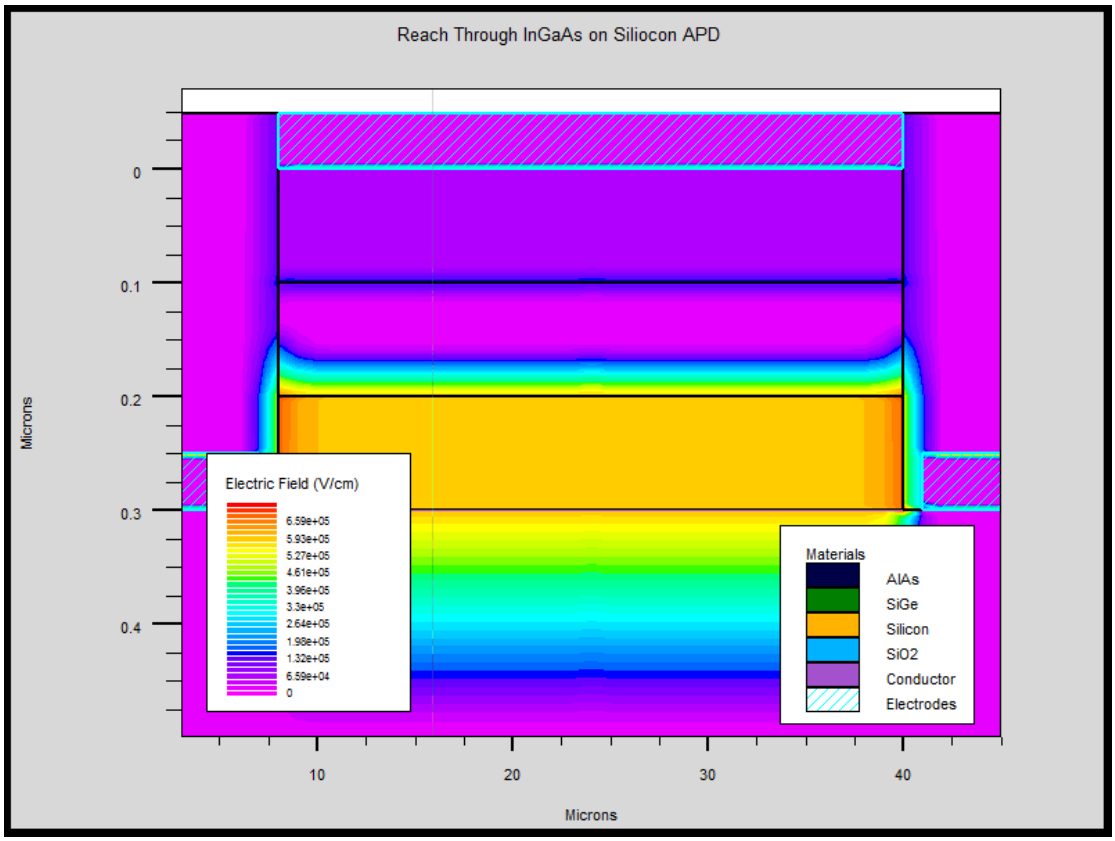

Figure 3.10 Electrical Filed A

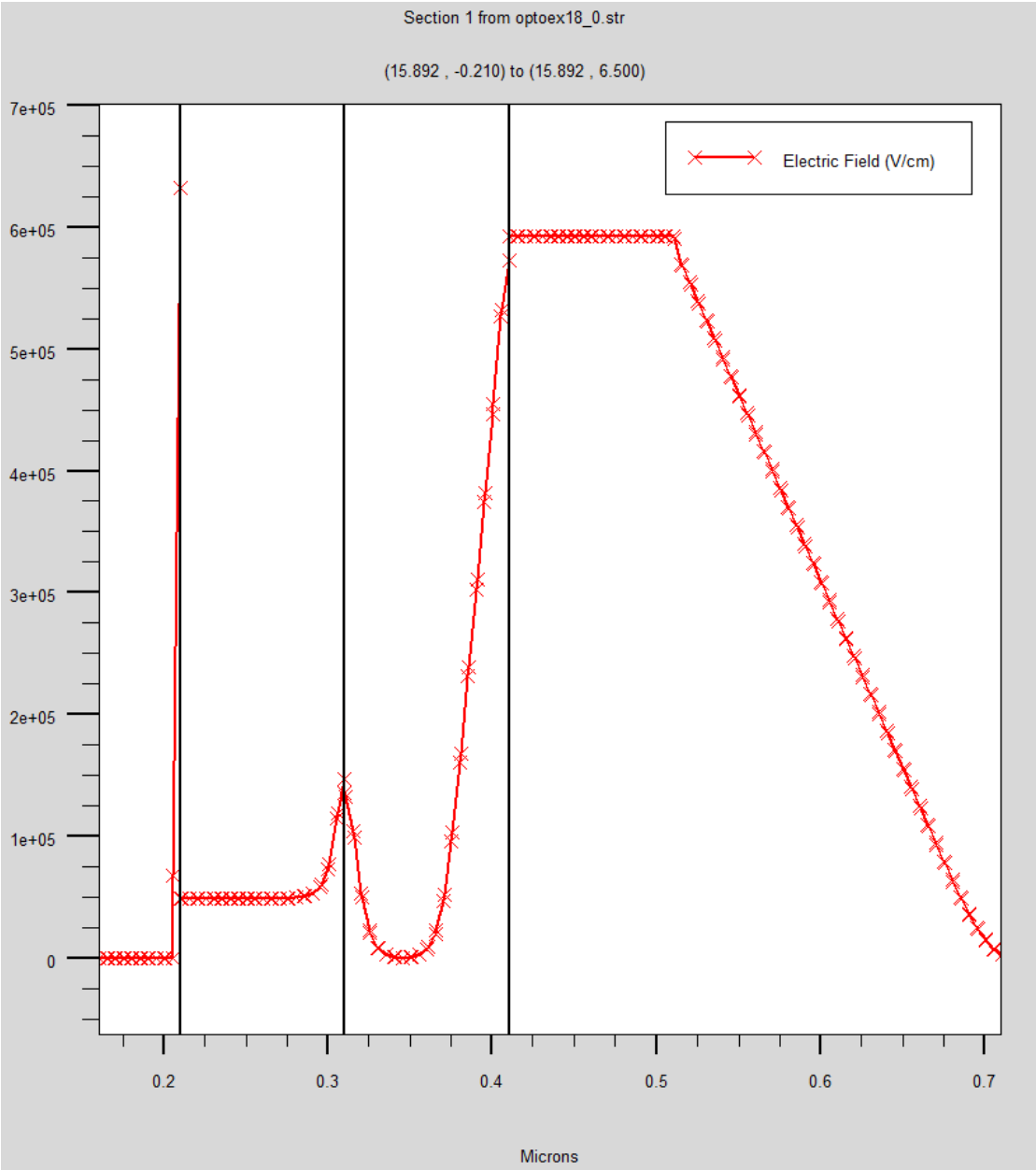

Figure 3.10 Electrical Filed B

Figure 3.11 Photogeneration rate

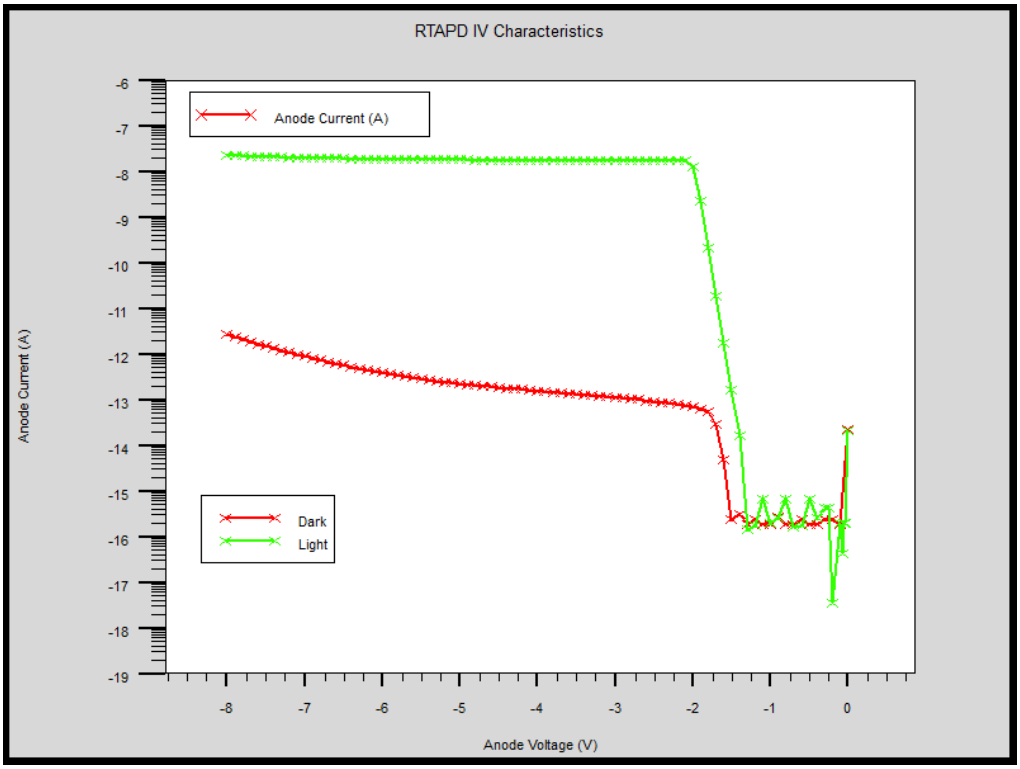

Figure 3.12Photogenerated current and Dark Current

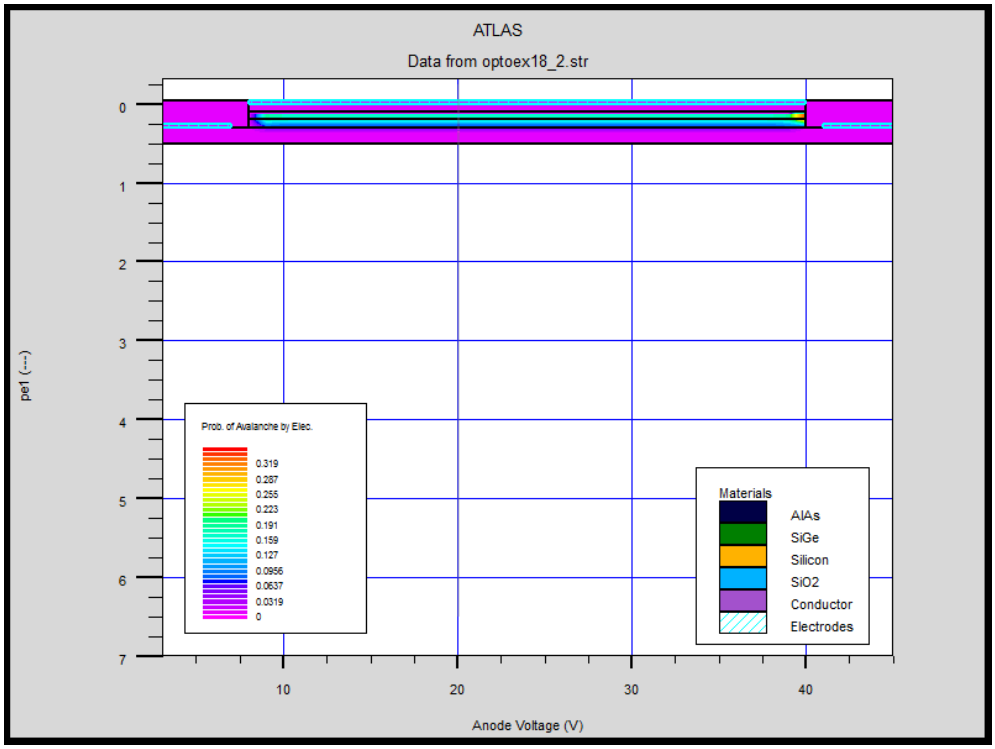

Figure 3.13 Avalanche rate

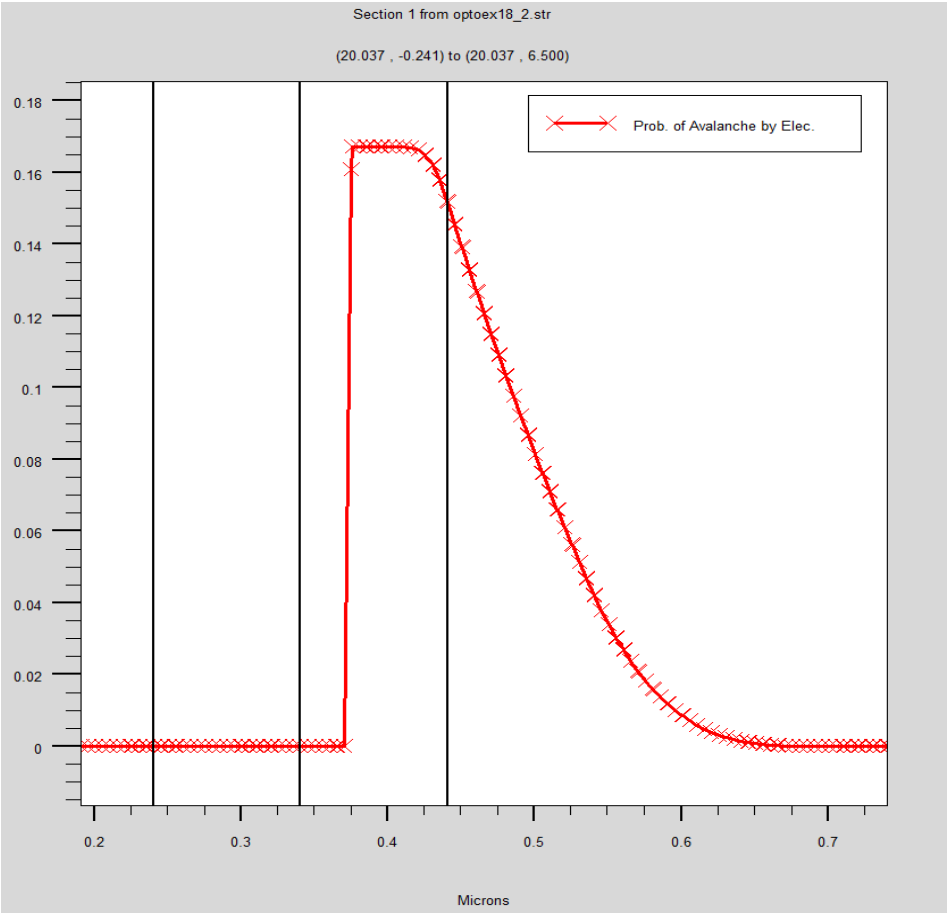

Figure 3.14 Electron Avalanche Possibilities

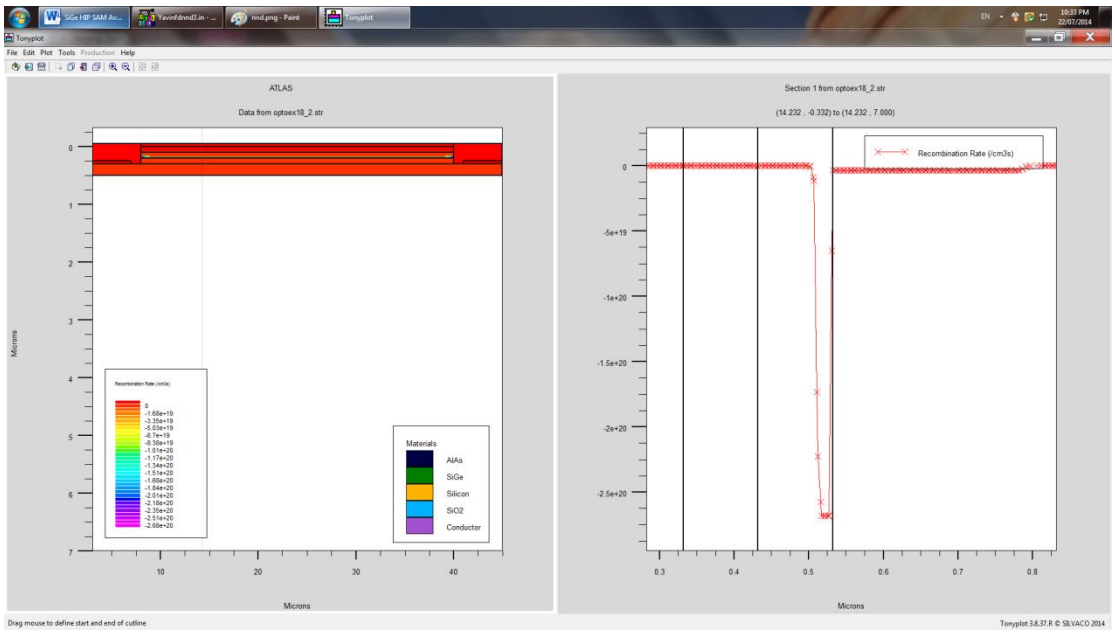

Figure 3.15 Recombination rate on x direction

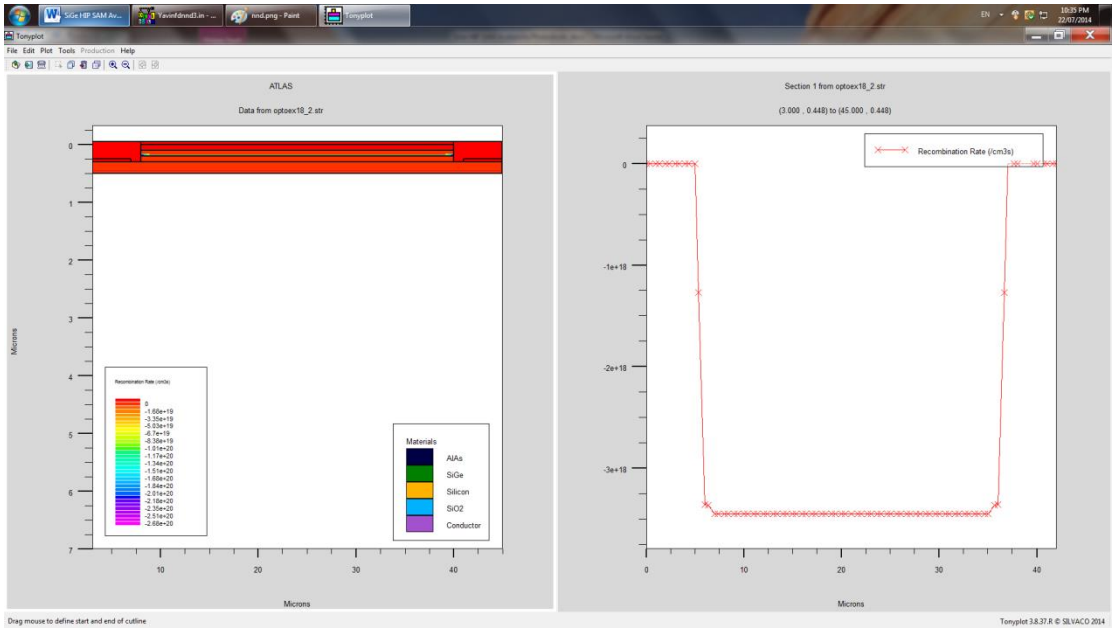

Figure 3.16 Figure 3.15 Recombination rate on y direction

By comparing the photogenerated current and dark in Figure 3.6, Figure 3.9 and Figure 3.13, the following advantages of designed SAM APDs could be concluded:

1 The output photocurrent is dependable on anode voltage.

2 The designed SiGe/Si HIP SAM APD can run at room temperature

3.6 Analysis of Dark Current and Generation-Recombination

The measured dark current of APDs can be viewed as the superposition of two main current components, i.e. the surface current component and the bulk current component [37]. In ideal APDs, the total dark current IdT can be expressed as a function of the multiplication factor M

$$I_{dT} = I_{dM} \times M + I_{d0}$$

where IdM × M and Id0 denote multiplied and unmultiplied dark current, respectively. The IdM × M is a volume contribution coming from the absorption and grading regions. It is produced by generated carriers that flow through the multiplication region under the p-n junction central region (48 μm in diameter) where the avalanche electric field is the maximum and impact ionization happens. The unmultiplied dark

current Id0 is identified as a combination of surface contribution as well as the contribution from the peripherical edge of the active region, where the electric field is lower than the central region of the junction and the multiplication is not expected to be built.

The IdM deduced from the volume contribution of IdT (i.e. IdM × M) can be quantitatively described by the sum of the three independent current sources: generation recombination of electron-hole pairs via traps in the depletion region (Igr), tunneling of carriers across the bandgap (Itun), and the diffusion current due to thermally generated minority carriers diffusing into the depletion region (Idiff) [10]. For the sake of simplicity, the tunneling via Shockley-Read-Hall (SRH) centers located within the bandgap was ignored and the shunt current was also neglected. Therefore, the theoretical components of the reverse dark current were proposed as below [12,13]

$$I_{gv} \doteq (qn_i Aw/\tau_{eff})[1-\exp(-\mathrm{qV}/2\,\mathrm{kT})]$$

$$I_{tun} \doteq \gamma A \exp(-\theta m_o^{1/2} \varepsilon_g^{3/2} / qhE_m)$$

$$I_{diff} = I_s[1-\exp(-qV/kT)]$$

where q is electronic charge, n_i is the intrinsic carrier concentration, A is the area of the active region, w is the depletion region width, τ_{eff} is the effective carrier lifetime, V is applied voltage, k is Boltzmann's constant, T is the temperature in Kelvin. In Eq. (3), m0 is the free-electron mass, E_m is the maximum junction electric field, is Planck's constant divided by 2p, and Eg is the energy gap. Other parametersare explained in [12] in detail. Is is the saturation current.

Chapter 4 Conclusions and Contributions

4.1 Conclusions

It is predicted that in IR region HgCdTe technology will continue in the future to expand the envelope of its capabilities because of its excellent properties. Despite serious competition from alternative technologies, HgCdTe is unlikely to be seriously challenged for high−performance applications, applications requiring multispectral capability and fast response. However, the non−uniformity is a serious problem in the case of LWIR and VLWIR HgCdTe detectors. For applications that require operation in the LWIR band as well as two colour MWIR/LWIR/VLWIR bands, most probably HgCdTe will not be the optimal solution [55].

New strategy in photodetector designs includes barrier detectors, unipolar barrier photodiodes and new p-n structures. It seems to be clear that certain of these solutions have merged as real competitions of HgCdTe photodetectors. The superior performance of barrier detector in comparison to conventional p−n junction photodiode is due to fact that the nBn structure is not limited by generation−recombination and tunneling currents. The low defect is the advantage of SiGe/Si HIP structure.

4.2 Contributions

The presented SiGe/Si HIP SAM MDIR PAD in this thesis shows some interesting simulation results such as the thickness of APD is very thin compare to few μm thickness of HgCdTe photodetector, the uniformity of designed APD is much better than that of HgCdTe photodetector, the room operating temperature is also another interesting aspect for this designed APD.

The three combined techniques are implemented into this MDIR photodetector design; some promising results are shown in this paper. Further research is needed to

optimize this MDIR photo detector design and 3D simulation can be implemented in furture.

References

1. A. Rogalski, *Infrared Detectors*, 2nd edition, CRC Press, Boca Raton, 2010.

2. A. White, “Infrared detectors”, U.S. Patent 4,679,063, 1983.

3. P.C. Klipstein, “Depletionless photodiode with suppressed dark current and method for producing the same”, U.S. Patent 7,795,640, 2003.

4. S. Maimon and G. Wicks, “nBn detector, an infrared detector with reduced dark current and higher operating temperature”, *Appl. Phys. Lett.* 89, 151109–1–3 (2006).

5. D.Z.−Y. Ting, A. Soibel, L. Hoglund, J. Nguyen, C.J. Hill, A. Khoshakhlagh, and S.D. Gunapala, “Type−II superlattice infrared detectors”, in *Semiconductors and Semimetals*, Vol.**84**, pp. 1–57, edited by S.D. Gunapala, D.R. Rhiger, and C. Jagadish, Elsevier, Amsterdam, 2011.

6. J.B. Rodriguez, E. Plis, G. Bishop, Y.D. Sharma, H. Kim, L.R. Dawson, and S. Krishna, “nBn structure based on InAs/GaSb type−II strained layer superlattices”, *Appl. Phys. Lett.* **91**, 043514−1–2 (2007).

7. G.R. Savich, J.R. Pedrazzani, D.E. Sidor, and G.W. Wicks, “Benefits and limitations of unipolar barriers in infrared photodetectors”, *Infrared Physics & Technol.* **59**, 152–155(2013).

8. P. Klipstein, “XBn barrier photodetectors for high sensitivityoperating temperature infrared sensors” *Proc. SPIE.* **6940**, 69402U−1–11 (2008).

9. D.Z. Ting, C.J. Hill, A. Soibel, J. Nguyen, S.A. Keo, M.C. Lee, J.M. Mumolo, J.K. Liu, and S.D. Gunapala, “Antimonide−based barrier infrared detectors”, *Proc. SPIE* **7660**,76601R−1–12 (2010).

10. P. Klipstein, O. Klin, S. Grossman, N. Snapi, I. Lukomsky, D. Aronov, M. Yassen,

A. Glozman, T. Fishman, E. Berkowicz, O. Magen, I. Shtrichman, and E. Weiss, "XB*n* barrier photodetectors based on InAsSb with high operating temperatures" *Opt. Eng.* **50**, 061002−1–10 (2011).

11. G.R. Savich, J.R. Pedrazzani, D.E. Sidor, S. Maimon, and G.W. Wicks, "Use of unipolar barriers to block dark currents in infrared detectors" *Proc. SPIE* **8012**, 8022T (2012).

12. P. Martyniuk and A. Rogalski, "HOT infrared photodetectors", *Opto−Electron. Rev*. **21**, 240−258 (2013).

13. P. Klipstein, D. Aronov, E. Berkowicz, R. Fraenkel, A. Glozman, S. Grossman, O. Klin, I. Lukomsky, I. Shtrichman, N.Snapi, M. Yassem, and E. Weiss, "Reducing the cooling requirements of mid−wave IR detector arrys", *SPIE Newsroom* 10.1117/2.1201111.003919, 2011.

14. M. Razeghi, S.P. Abdollahi, E.K. Huang, G. Chen, A. Haddadi, and B.M. Nquyen, "Type−II InAs/GaSb photodiodes and focal plane arrays aimed at high operating temperatures", *Opto−Electr. Rev*. **19**, 261–269 (2011).

15. M. Razeghi, "Type II superlattice enables high operating temperature," *SPIE Newsroom*, 10.1117/2.1201110.003870 (2011).

16. G.R. Savich, J.R. Pedrazzani, D.E. Sidor, S. Maimon, and G.W. Wicks, "Dark current filtering in unipolar barrier infrared detectors", *Appl. Phys. Lett*. **99**, 121112 (2011).

17. P.C. Klipstein, Y. Gross, A. Aronov, M. ben Ezra, E. Berkowicz, Y. Cohen, R. Fraenkel, A. Glozman, S. Grossman,O. Kin, I. Lukomsky, T. Markowitz, L. Shkedy, I. Sntrichman, N. Snapi, A. Tuito, M. Yassen, and E. Weiss, "Low SWaP MWIR detector based on XBn focal plane array" *Proc. SPIE* **8704**, id. 87041S−1−12 (2013).

144 Opto−Electron. Rev., **22**, no. 2, 2014 c 2014 SEP, Warsaw

18. A. Khoshakhlagh, S. Myers , E. Plis , M.N. Kutty, B. Klein, N. Gautam, H. Kim, E.P.G. Smith, D. Rhiger, S.M. Johnson, and S. Krishna, “Mid−wavelength InAsSb detectors based on nBn design”, *Proc. SPIE* **7660**, 76602Z (2010).

19. A.M. Itsuno, J.D. Philips, and S. Velicu, “Design and modelling of HgCdTe nBn detectors”, *J. Elect. Mater*. **40**,1624–1629 (2011).

20. M. Kopytko, A. Kębłowski, W. Gawron, P. Madejczyk, A.Kowalewski, and K. Jóźwikowski, “High−operating temperature MWIR nBn HgCdTe detector grown by MOCVD”,*Opto−Electr. Rev.* **21**. 42, 402−405 (2013).

21. J.F. Klem, J.K. Kim, M.J. Cich, S.D. Hawkins, T.R. Fortune, and J.L. Rienstra, “Comparison of nBn and nBp mid−wavebarrier infrared photodetectors”, *Proc. SPIE* **7608**, 76081P(2010).

22. H. Kroemer, “The 6.1 _ family (InAs, GaSb, AlSb) and itsheterostructures: a selective review”, *Physica* **E**20, 196–203(2004).

23. H. Sakaki, L.L. Chang, R. Ludeke, C.A. Chang, G.A. SaiHalasz, and L. Esaki, “In1−xGaxAs−GaSb1−yAsy heterojunctions by molecular beam epitaxy”, *Appl. Phys. Lett*. **31**, 211–213 (1977).

24. Y. Wei and M. Razeghi, “Modelling of type−II InAs/GaSb superlattices using an empirical tight−binding method and interface engineering”, *Phys. Rev*. **B69**, 085316−7 (2004).

25. G.A. Umana−Membreno, B. Klein, H. Kala, J. Antoszewski, N. Gautam, M.N. Kutty, E. Plis, S. Krishna, and L. Faraone,“Vertical minority carrier electron transport in p−type InAs/GaSb type−II superlattices”, *Appl Phys. Lett*. **101**, 253515(2012).

26. D. Zuo, P. Qiao, D. Wasserman, and S.L. Chuang, “Direct observation of minority carrier lifetime improvement in InAs/GaSb type−II superlattice photodiodes via interfacial layer control”, *Appl. Phys. Lett.* **102**, 141107 (2013).

27. E. Weiss, O. Klin, S. Grossmann, N. Snapi, I. Lukomsky, D.ronov, M. Yassen, E. Berkowicz, A. Glozman, P. Klipstein, A. Fraenkel, and I. Shtrichman, “InAsSb−based XBnn bariodes grown by molecular beam epitaxy on GaAs”, *J.*

28. P. Martyniuk and A. Rogalski, “Modelling of InAsSb/AlAsSbnBn HOT detector's performance limits”, *Proc. SPIE* **8704**,87041X (2013).

29. A.I. D’Souza, E. Robinson, A.C. Ionescu, D. Okerlund, T.J. de Lyon, R.D. Rajavel, H. Sharifi, N.K. Dhar, P.S. Wijewarnasuriya, and C. Grein, “5MWIR InAsSb barrier detector data and analysis”, *Proc. SPIE* **8704**, 87041U (2013).

30. E.H. Aifer, J.G. Tischler, J. H. Warner, I. Vurgaftman, W.W. Bewley, J.R. Meyer, J.C. Kim, and L.J. Whitman, “W−structured type−II superlattice long−wave infrared photodiodes with high quantum efficiency”, *Appl. Phys. Lett*. **89**, 053519(2006).

31. B.−M. Nguyen, M. Razeghi, V. Nathan, and G.J. Brown, “Type−II “M” structure photodiodes: an alternative material design for mid−wave to long wavelength infrared regimes”, *Proc. SPIE* **6479**, 64790S (2007).

32. B.−M. Nguyen, D. Hoffman, P.−Y. Delaunay, and M. Razeghi, “Dark current suppression in type II InAs/GaSb superlattice long wavelength infrared photodiodes with M−structure”, *Appl. Phys. Lett*. 163511 (2007).

33. B.−M. Nguyen, D. Hoffman, P.−Y. Delaunay, E.K. Huang, M.Razeghi, and J. Pellegrino, “Band edge tunability of *M*−structure for heterojunction design in Sb based type II superlattice photodiodes”, *Appl. Phys. Lett*. **93**, 163502 (2008).

34. M. Razeghi, H. Haddadi, A.M. Hoang, E.K. Huang, G. Chen, S. Bogdanov, S.R. Darvish, F. Callewaert, and R. McClintock, “Advances in antimonide−based Type−II superlattices for infrared detection and imaging at centre for quantum devices”, *Infrared Phys. & Technol.* **59**, 41–52 (2013).

35. O. Salihoglu, A. Muti, K. Kutluer, T. Tansel, R. Turan, Y.Ergun, and A. Aydinli,

"≪N≫ structure for type−II superlattice photodetectors", *Appl. Phys. Lett*. **101**, 073505 (2012).

36. J.L. Johnson, L.A. Samoska, A.C. Gossard, J.L.Merz, M.D. Jack, G.H. Chapman, B.A. Baumgratz, K. Kosai, and S.M. Johnson, "Electrical and optical properties of infrared photodiodes using the InAs/Ga1–xInxSb superlattice in heterojunctions with GaSb", *J. Appl. Phys.* **80**, 1116–1127 (1996).

37. A. Khoshakhlagh J.B. Rodriguez, E. Plis, G.D. Bishop, Y.D.Sharma, H.S. Kim, L.R. Dawson and S. Krishna, "Bias dependent dual band response from InAs/Ga(In)Sb type II strain layer superlattice detectors", *Appl. Phys. Lett*. **91**263504 (2007).

38. S.D. Gunpala, D.Z Ting, C.J. Hill, and S.V. Bandara, *U.S. Patent* No. 7,737,411, 2010.

39. N.D. Akhavan, G. Jolley, G. Umana−Membreno, J. Antoszewski, and L. Faraone, "Performance modelling of bandgap engineered HgCdTe−based nBn infrared detectors", *Extended Abstracts, The 2013 Workshop on the Physics and Chemistry of II–VI Materials*, Chicago (2013).

40. M. Kopytko, A. Kębłowski, W. Gawron, A. Kowalewski,"MOCVD grown HgCdTe barrier structures for high−operating temperature MWIR photodetectors", to be published.

41. L. Zheng, M. Tidrow, L. Aitcheson, J. O'Connor, and S. Brown, "Developing high performance III−V superlattice IRFPAs for defense – challenges and solutions", *Proc. SPIE* **7660**, 7660−1–12 (2010).

42. C.J. Hill, A. Soibel, S.A. Keo, J.M. Mumolo, D.Z. Ting, S.D. Gunapala, D.R. Rhiger, R.E. Kvaas, and S.F. Harris, "Demonstration of mid and long−wavelength infrared antimonide−based focal plane arrays", *Proc. SPIE* **7298**, 7294–04 (2009).

43. S.D. Gunapala, D.Z. Ting, C.J. Hill, J. Nguyen, A. Soibel,S.B. Rafol, S.A. Keo, J.M. Mumolo, M.C. Lee, J.K. Liu, and B. Yang, “Demonstration of a 1024×1024 pixel InAs−GaSb superlattice focal plane array”, *Phot. Tech. Lett*. **22**, 1856–1858 (2010).

44. P. Manurkar, S. Ramezani−Darvish, B.−M. Nguyen, M. Razeghi, and J. Hubbs, “High performance long wavelength infrared mega−pixel focal plane array based on type−II superlattices”, *Appl. Phys. Lett*. **97**, 193505−1–3 (2010).

45. A. Rogalski, J. Antoszewski, and L. Faraone, “Third−generation infrared photodetector arrays”, *J. Appl. Phys.* **105**,091101 (2009).

46. A.M. Hoang, G. Chen, A. Haddadi, and M. Razeghi, “Demnstration of high performance bias−selectable dual−band short−/mid−wavelength infrared photodetectors based on type−II InAs/GaSb/AlSb superlattices”, *Appl. Phys. Lett.* **102**,011108 (2013).

47. M. Razeghi, A.M. Hoang, A. Haddadi, G. Chen, S. Ramezani−Darvish, P. Bijjam, P. Wijewarnasuriya, and E. Decuir,“High−performance bias−selectable dual−band short−/Midwavelength infrared photodetectors and focal plane arrays based on InAs/GaSb/AlSb type−II superlattices”, *Proc. SPIE* **8704**, 8704–54 (2013).

48. M. Razeghi, A. Haddadi, A.M. Hoang, G. Chen, S. Ramezani−Darvish, and P. Bijjam, “High−performance bias−selectable dual−band mid−/long−wavelength infrared photodetectors and focal plane arrays based on InAs/GaSb type−II superlattices”, *Proc. SPIE* **8704**, 87040S (2013).

49. M.A. Kinch, H.F. Schaake, R.L. Strong, P.K. Liao, M.J. Ohlson, J. Jacques, C−F Wan, D. Chandra, R.D. Burford, and C.A. Schaake, “High operating temperature MWIR detectors”, *Proc. SPIE* **7660**, 76602V−1 (2010).

50. W.W. Bewley, J.R. Lindle, C.S. Kim, M. Kim, C.L. Canedy, I. Vurgaftman, and

J.R. Meyer, “Lifetime and Auger coefficients in type−II W interband cascade lasers”, *Appl. Phys. Lett.* **93**, 041118 (2008).

51. M.A. Kinch, *Fundamentals of Infrared Detector Materials,* SPIE Press, Bellingham, 2007.

52. M.A. Kinch, ”The challenges of background limited room temperature photon detection”, *The 2013 U.S. Workshop on the Physics and Chemistry of II−VI Materials*, Tutorial Session, Chicago, 2013.

53. J. Wrobel, P. Martyniuk, E. Plis, P. Madejczyk, W. Gawron, S. Krishna, and A. Rogalski, “Dark current modeling of MWIR type−II superlattice detectors”, *Proc. SPIE* **8353**, 8353–16 (2012).

54. http://www.laserfocusworld.com/articles/print/volume-48/issue 04/features/microbolometer-arrays-enable-uncooled-infrared-camera.html

55. http://www.photonics.com/Article.aspx?AID=22475

56. http://www.octsensors.com/cds/p6-12.htm

57. http://hamamatsu.magnet.fsu.edu/articles/avalanche.html

58. Resonant normal-incidence separate-absorption-charge-multiplication Ge/Si avalanche photodiodes; Daoxin Dai, Hui-Wen Chen, John E. Bowers, Yimin Kang, Mike Morse, and Mario J. Paniccia Optics Express, Vol. 17, Issue 19, pp. 16549-16557 (2009)